PHYSICAL REVIEW E **74**, 051403 (2006)

Viscous froth lens

T. E. Green, A. Bramley, L. Lue, and P. Grassia*
SCEAS, The University of Manchester, P.O. Box 88, Sackville Street, Manchester M60 1QD, United Kingdom

(Received 5 May 2006; revised manuscript received 2 August 2006; published 13 November 2006)

Microscale models of foam structure traditionally incorporate a balance between bubble pressures and surface tension forces associated with curvature of bubble films. In particular, models for flowing foam microrheology have assumed this balance is maintained under the action of some externally imposed motion. Recently, however, a dynamic model for foam structure has been proposed, the viscous froth model, which balances the net effect of bubble pressures and surface tension to viscous dissipation forces: this permits the description of fast-flowing foam. This contribution examines the behavior of the viscous froth model when applied to a paradigm problem with a particularly simple geometry: namely, a two-dimensional bubble "lens." The lens consists of a channel partly filled by a bubble (known as the "lens bubble") which contacts one channel wall. An additional film (known as the "spanning film") connects to this bubble spanning the distance from the opposite channel wall. This simple structure can be set in motion and deformed out of equilibrium by applying a pressure across the spanning film: a rich dynamical behavior results. Solutions for the lens structure steadily propagating along the channel can be computed by the viscous froth model. Perturbation solutions are obtained in the limit of a lens structure with weak applied pressures, while numerical solutions are available for higher pressures. These steadily propagating solutions suggest that small lenses move faster than large ones, while both small and large lens bubbles are quite resistant to deformation, at least for weak applied back pressures. As the applied back pressure grows, the structure with the small lens bubble remains relatively stiff, while that with the large lens bubble becomes much more compliant. However, with even further increases in the applied back pressure, a critical pressure appears to exist for which the steady-state structure loses stability and unsteady-state numerical simulations show it breaks up by route of a topological transformation.

DOI: 10.1103/PhysRevE.74.051403 PACS number(s): 83.80.Iz, 82.70.Rr, 83.50.Ha

I. INTRODUCTION

Foams are non-Newtonian fluids which acquire their complex rheological behavior [1–3] as a result of their microstructure. Specifically this microstructure consists of a dispersed phase (gas bubbles) separated by a continuous phase (made up of thin liquid films). Surface tension at the phase interfaces leads to an energy penalty according to the total amount of surface between the phases. Stationary (i.e., not flowing) foams thus seek a (local) minimum of surface area (three-dimensional case) or surface perimeter (two-dimensional case) to keep the surface energy low [4,5].

When foams are subjected to some externally imposed strain, the microstructure deforms: both surface area and surface energy increase. For small imposed strains, despite this energy increase, bubbles tend to maintain their positions relative to their neighbors and the original state is recoverable if the strain is released. For larger imposed strains, bubbles rearrange [3,6]: the topology changes as bubbles lose contact with their original neighbors and make contact with new ones. Following these so-called *topological transformations*, even as the imposed strain is released, the original state is not necessarily recovered.

These features have been elucidated in a number of simulation studies, in both two-dimensions [1,7–12] and three dimensions [13–16]. However, the above-mentioned simulations restrict consideration to slow flowing (i.e., quasistatic) foams. Specifically they compute the foam microstructure as a constrained energy minimization problem subject to some imposed incremental boundary motion. In the minimum-energy state, net surface tension forces normal to films (associated with film curvatures) need to be matched to pressure differences across films (Lagrange multipliers in the energy minimization associated with maintaining specified bubble volumes): formal mathematical derivations and manipulations of this result based on the Lagrange multiplier formalism are available [17,18]. The quasistatic computations do not consider cases where the foam is subject to rapid imposed strains, driving, and/or maintaining it far from its minimum-energy state. In such cases, experiments [19–21] and theory [22,23] show a marked change in the rheology as strain rate increases: the microscale bubble motion switches from being intermittent to continuous, with dissipative forces smoothing the flow. The foam structure is also altered [24] in the more rapid strain rate limit: energy-relaxing topological transformations tend to be suppressed [1], implying foam films should be elongated to a much greater extent than for an equivalent strain that is imposed slowly. This effect has been seen clearly in experiment [21].

There are also technical difficulties with implementing the quasistatic simulations as, at the topological transformation, the foam effectively jumps from one energy minimum to another. Occasionally this triggers an avalanche of other transformations [6,16,25], and it is not entirely clear in a simulation in which order these should be applied. Moreover, the system can occasionally jump back and forth between topological states [26], only definitively settling into one particular state as further strain increments are imposed.

All these drawbacks have driven the search for new models of foam structure and dynamics, which can (i) resolve

---

*Electronic address: paul.grassia@manchester.ac.uk topological transformations over a finite (typically small) increment of imposed strain, instead of treating them as discrete jumps, (ii) assign a definite order to events occurring during bubble rearrangement avalanches, and (iii) describe rapidly strained and far-from-equilibrium foams, in terms of both their dynamics and structure.

Various models in the literature have been developed to address the above issues. A Monte Carlo lattice-based Ising model, known as the Potts model [6], seems to give reasonable phenomenological behavior. However, the dynamics is described in terms of Monte Carlo steps: it is far from obvious how to relate such steps to an actual relaxation time scale set by dissipative forces in a real foam. Another attempt is the so-called bubble model [22,23,27], which treats bubbles as (possibly slightly overlapping) circles (two dimensions) or spheres (three dimensions). The bubbles experience elastic forces according to the extent they overlap and also viscous dissipation according to their motion relative to each other and/or to some average imposed flow. The virtue of the bubble model is its computational simplicity, but it is really only applicable to wet foams: it makes no attempt to describe highly elongated or deformed bubbles which are far from circular or spherical. Yet another useful model is the vertex model [12,28], which treats bubbles as straight-edged objects joined by vertices. Rapid flow involving viscous dissipation forces can be incorporated (dissipation being tied to the vertices) even though early work on the model [12] did not concern itself with this regime. The vertex model, however, suffers some of the limitations of the bubble model in terms of describing bubble structures: the geometric shapes of the bubbles are not realistic, films (through the model's inability to represent their curvature) failing to meet each other at the angles they should.

In view of the limitations discussed above, one model which has gained popularity in recent years is the so-called viscous froth model [29–34]. The model still retains the forces mentioned earlier: namely, the film curvature forces (induced by surface tension) and the pressure forces across films. However, it no longer equates them; rather, it says that any mismatch between them produces film motion. A force balance then results through equating a viscous drag force associated with this film motion to the sum of pressure and curvature forces. Thus

$$\zeta v_{\perp} = \Delta p - 2\sigma\kappa, \tag{1}$$

where ζ is a viscous drag coefficient, $v_{\perp}$ is the velocity of an element of film in the normal direction, Δp is the pressure difference across the film, σ is surface tension, and κ is film curvature.

Some comments concerning the model are relevant. Throughout this work, we envisage that Eq. (1) applies to a two-dimensional foam: physically this would be realized by confining a foam between closely spaced glass plates. The precise shape of the films in a foam thus confined, and the context in which this system can be considered effectively two dimensional is quite subtle: details may be found in Appendix A. We also envisage that the foam is dry; i.e., its liquid fraction is exceedingly small. Viewed from above the confining plates, the foam films are now curves in the plane, while the bubbles have a specified area (not volume). Applied to a bubble with no externally imposed strain, it is relatively simple to see how Eq. (1) behaves: if a film is not initially an arc of a circle, so that κ is spatially nonuniform, film elements move, tending to relax κ to the uniform value $\Delta p/(2\sigma)$. The reason 2σ, not merely σ, appears is because the film tension is twice the surface tension, each film having two surfaces. The rate of this relaxation process is governed by the drag coefficient ζ. The drag forces are realized by the films sweeping across the confining plates: in its simplest form the drag force can be assumed linear in the film velocity, although certain power law relations may in fact be more realistic [12,35–39]: see also Appendix B.

The viscous froth model has had a number of notable successes in recent years, being applied to foam relaxation after film bursting [31,32], Taylor-Couette flow of foam [32,33], and foam flows in channels [31,32,34].

In particular, channel flow studies have reproduced the result of a two-dimensional experiment in which a bubble train is pushed through a curved channel. The bubble train is arranged into a so-called staircase structure; i.e., it is stacked two bubbles deep across the channel and several bubbles deep along the channel. The experimental observation is that for slow-moving trains, bubbles exit the curved channel in the same order that they entered it. However, for fast-moving trains, some bubbles overtake others, undergoing a topological transformation as the curve is negotiated. As the topological transformation is dependent on the rate of motion imposed on the train, it is essential to describe it using a rate-sensitive model such as Eq. (1). If a quasisteady balance between pressure and surface curvature forces were assumed, no transformation would be predicted.

The present study has been motivated by these bubble train experiments. The aim is to see whether a bubble train could have any interesting behavior even in a perfectly straight channel. In the interests of simplicity we consider only the simplest nontrivial train. This consists of a single bubble partially filling the width of the channel, with semi-infinite bubbles in front of and behind it (a more detailed description of the structure will be given later; see also Figs. 1 and 2). For reasons to become apparent shortly, we call this configuration a *lens* structure.

We will subject the lens structure to a driving force setting it into motion, while also deforming it. As we shall demonstrate, the lens has a very interesting dynamical behavior as a function of the strength of the driving force. We shall be particularly interested in how the structure deforms and elongates, because film elongation in foam is associated with more surface energy and, in rheological terms, more stress [1]. Overall the present study will elucidate the very rich physics embedded within the viscous froth model.

This paper is arranged as follows. In the next section we compute the properties of an equilibrium lens—i.e., one that is stationary. Then in Sec. III we set up the equations for a moving lens which is assumed to be steadily migrating. In Sec. IV we consider the case of a weakly driven lens. After that we describe how to move from the weakly driven to the strongly driven state by following a steady solution branch. However, it appears that a steadily migrating lens is only possible up to a given driving force. This leads in Sec. VI to

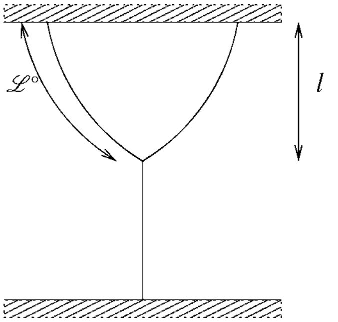

FIG. 1. The equilibrium lens shape assuming a unit width channel. The parameter l is the relative distance that the equilibrium lens extends across the channel (measured in terms of the channel width, which we take to be unity here) and is related to the equilibrium lens area, pressure, and surface energy [see Eqs. (2), (4), and (5)]. The parameter l is also directly related to the length of each curved arm of the lens bubble, $\mathcal{L}^\circ$, via $\mathcal{L}^\circ = 2\pi l/(3\sqrt{3})$ [Eq. (3)].

the discovery of a second (steady) branch of solutions. The unsteady state of the lens is analyzed in Sec. VII: it appears that the original solution branch is in fact the stable one. For larger driving forces, the lens structure breaks up via a topological transformation. Conclusions are offered in Sec. VIII. Some derivations which are particularly mathematical are confined to Appendixes A–E at the end of the paper.

II. EQUILIBRIUM LENS

Consider a long straight channel of width L drawn in the plane. Consider also a (two-dimensional) bubble confined near one wall of the channel. An additional film (hereafter called the spanning film) attaches to the bubble spanning the distance across the channel to the opposite wall. The system is allowed to relax to its equilibrium state (i.e., it is not driven in any way), and suppose that, at equilibrium, the bubble occupies a fraction l of the channel width, the spanning film therefore occupying a fraction $1-l$. The equilibrium state is sketched in Fig. 1: clearly l is determined by the bubble area. As can be seen, the bubble is stretched out into a cusped shape much like a lens; hence, we call this simple configuration a *lens* structure.

All films must leave the channel walls at right angles: otherwise an unbalanced force along the wall would arise. In the equilibrium state, the spanning film is flat, while the two films of the bubble (hereafter referred to as the front and back films) are mirror images of each other. The front and back films are arcs of circles, each subtending an angle of $\frac{\pi}{3}$. This enables all three films to meet at the vertex at $\frac{2\pi}{3}$ as required by Plateau's law for foam.

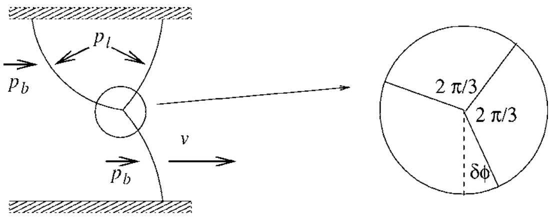

FIG. 2. A distorted lens driven by an imposed back pressure p_b and traveling at some (unknown) migration velocity v. The so-called spanning film turns through an (unknown) angle $\delta\phi$, but all films still meet at $\frac{2\pi}{3}$ angles at the vertex (see the close-up view of the vertex on the right of the figure). The lens pressure p_l is also affected.

We elect to make all distances dimensionless on the scale L, bubble areas dimensionless on the scale L^2, film curvatures dimensionless on the scale L^{-1}, bubble pressures dimensionless on the scale $2\sigma/L$, and surface energies (per unit thickness of the gap between the glass plates confining the two-dimensional foam) dimensionless on the scale $2\sigma L$.

Taking into account the above considerations and applying some elementary geometry and trigonometry, we deduce the following relations between the equilibrium lens extent l, the area of the lens bubble A_l, the individual film lengths on the front and back of the lens bubble $\mathcal{L}^\circ$, the equilibrium pressure of the lens bubble p_l°, and the equilibrium surface energy E°:

$$A_l = \left(\frac{4\pi}{9} - \frac{1}{\sqrt{3}}\right) l^2, \tag{2}$$

$$\mathcal{L}^\circ = 2\pi l/(3\sqrt{3}), \tag{3}$$

$$p_l^\circ = \sqrt{3}/(2l), \tag{4}$$

$$E^\circ = 2\mathcal{L}^\circ + 1 - l = \left(\frac{4\pi}{9} - \frac{1}{\sqrt{3}}\right)\sqrt{3}l + 1, \tag{5}$$

where the pressure outside the lens has been set to zero, with no loss of generality.

This completes the analysis of an equilibrium lens. In the next section we will consider what happens as the lens is driven out of equilibrium.

III. STEADY STATE OF VISCOUS FROTH LENS

Now we assume that a (dimensionless) back pressure p_b is imposed behind the lens, the pressure in front of the lens remaining zero. The spanning film will now curve, the symmetry between the front and back film will be broken, the lens pressure will deviate from p_l°, and the lens will be set into motion. The aim of this section is to derive equations for the extent of curvature of the spanning film, the deviation of the lens pressure from equilibrium, and the overall velocity of motion, assuming the lens structure, albeit distorted, migrates at a steady rate. The actual solutions of the equations we derive will be obtained and analyzed in later sections.

We retain dimensionless scales defined in Sec. II and additionally make velocity dimensionless on the scale $2\sigma/(L\zeta)$. We also make time dimensionless on the scale $L^2\zeta/(2\sigma)$, although we shall deal with a steady-state analysis in the first instance (see Appendix B for an estimate of how big these scales would be in a real physical system).

The (dimensionless) equation of the viscous froth is now

$$v_{\perp} = \Delta p - \kappa, \tag{6}$$

where $v_{\perp}$ is the film velocity locally normal to the film, Δp is the pressure difference across the film, and κ is film curvature.

We parametrize the films by a so-called "turning angle" ϕ. Specifically, ϕ is the angle through which the film tangent has turned with respect to the direction it had at the channel wall. As in Sec. II, we continue to assume that films meet the channel walls at right angles so as to avoid unbalanced forces there: the viscous froth model *in its simplest form* associates drag only with film elements, not with the end points of films. Remember that the two-dimensional viscous froth represents a foam confined between two closely spaced glass plates: neglect of drag on film end points then assumes that the plate separation is arbitrarily small compared to the film lengths and/or the span of the channel. Recent experiments suggest that, fixing the plate separation to channel span aspect ratio, additional drag forces on film end points should in fact be added to the viscous froth model, particularly for rapidly migrating structures [34]. The drag force required where a film end point meets a channel wall is equivalent to the drag on a segment of viscous froth film with a length equal to half the plate separation. The reason for the factor of $\frac{1}{2}$ is that the equivalent segment confined between two glass plates would have drag on both upper and lower plates.

Here, as stated above, we shall ignore such complications. One of the main effects we shall predict, even with our current model, is the tendency of the lens bubble to lag behind the spanning film as the structure migrates owing to the lens bubble having more films and hence more drag per unit height: incorporating additional drag on film end points should only enhance this tendency.

The total angle through which the spanning film turns (from channel wall to vertex) will be denoted $\delta\phi$, so that $0 \leq \phi \leq \delta\phi$ for the spanning film (see Fig. 2). Since all films meet at the vertex at $\frac{2\pi}{3}$ angles, the back film has $0 \leq \phi \leq \frac{\pi}{3} + \delta\phi$ and the front film has $-\frac{\pi}{3} + \delta\phi \leq \phi \leq 0$. Our immediate objective is to express the coordinates of points on films as functions of ϕ over these ranges, since this will subsequently enable us to formulate constraint equations which govern the overall film distortion, pressure in the lens bubble, and steady migration velocity.

A. Obtaining film coordinates in terms of turning angle

Toward the above stated objective, the film curvature can be readily expressed in terms of the turning angle ϕ and distance s along the film:

$$\kappa = \frac{d\phi}{ds}. \tag{7}$$

We measure s from below, so that κ is positive on the front and spanning films and is negative on the back film.

A film whose local orientation is ϕ and which displaces by an amount $v_{\perp} dt$ has an *apparent* horizontal displacement $v_{\perp} dt/\cos\phi$ (see Fig. 3). If the lens is at steady state—i.e., propagating along the channel without change of shape—then it has an apparent propagation speed v which is uniform across the entire structure. Thus

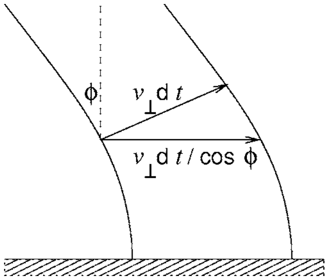

FIG. 3. A local element of film which has turned through an angle ϕ relative to its (vertical) orientation at the channel wall. In a time dt, the film displaces in the normal direction by an amount $v_{\perp} dt$, while the apparent horizontal displacement of the structure is $v_{\perp} dt/\cos\phi$.

$$v = v_{\perp}/\cos\phi. \tag{8}$$

If we substitute Eq. (7) and (8) into Eq. (6) (and rearrange), we obtain

$$\frac{ds}{d\phi} = \frac{1}{\Delta p - v\cos\phi}. \tag{9}$$

An element of film ds which is curved back through an angle ϕ relative to the vertical can be decomposed into Cartesian components $dy = \cos\phi\, ds$ and $dx = -\sin\phi\, ds$. Thus

$$\frac{dy}{d\phi} = \frac{\cos\phi}{\Delta p - v\cos\phi}, \tag{10}$$

$$\frac{dx}{d\phi} = -\frac{\sin\phi}{\Delta p - v\cos\phi}. \tag{11}$$

We shall denote the values of x and y from Eqs. (10) and (11) with subscripts s, b, and f according to whether they refer to the spanning, back, or front films. As we know the values of y when $\phi=0$ for all three films ($y_s=0$ and $y_b=y_f=1$), it is convenient to integrate Eq. (10). In this equation, we shall also employ the aforementioned subscripts s, b, and f on the film pressure differences Δp, these pressure differences being measured from behind to in front.

Before proceeding, we define three parameters, denoted a_s, a_b, and a_f, which are ratios of film velocities to driving pressures (as such these can be thought of as film mobility parameters):

$$a_s = \frac{v}{(\Delta_s p)} = \frac{v}{p_b}, \tag{12}$$

$$a_b = -\frac{v}{(\Delta_b p)} = \frac{v}{(p_l - p_b)}, \tag{13}$$

$$a_f = \frac{v}{(\Delta_f p)} = \frac{v}{p_l}. \tag{14}$$

Note that in the limit of weakly driven films, a_s, is order unity, while a_b and a_f are small parameters. The signs have been chosen to ensure a_s, a_b, and a_f are positive in that same limit.

Thus we obtain from Eq. (10) for the three films

$$\frac{dy_s}{d\phi} = \frac{1}{v}\frac{a_s\cos\phi}{(1 - a_s\cos\phi)} = \frac{1}{v}\left(-1 + \frac{1}{1 - a_s\cos\phi}\right), \tag{15}$$

$$\frac{dy_b}{d\phi} = -\frac{1}{v}\frac{a_b\cos\phi}{(1 + a_b\cos\phi)} = \frac{1}{v}\left(-1 + \frac{1}{1 + a_b\cos\phi}\right), \tag{16}$$

$$\frac{dy_f}{d\phi} = \frac{1}{v}\frac{a_f\cos\phi}{(1 - a_f\cos\phi)} = \frac{1}{v}\left(-1 + \frac{1}{1 - a_f\cos\phi}\right). \tag{17}$$

After integration, we obtain

$$y_s = \frac{1}{v}\left\{-\phi + \frac{2}{(1 - a_s^2)^{1/2}}\arctan\left[\left(\frac{1 + a_s}{1 - a_s}\right)^{1/2}\tan\frac{\phi}{2}\right]\right\},$$

$$0 \le \phi \le \delta\phi, \tag{18}$$

$$y_b = 1 + \frac{1}{v}\left\{-\phi + \frac{2}{(1 - a_b^2)^{1/2}}\arctan\left[\left(\frac{1 - a_b}{1 + a_b}\right)^{1/2}\tan\frac{\phi}{2}\right]\right\},$$

$$0 \le \phi \le \frac{\pi}{3} + \delta\phi,\ |a_b| < 1, \tag{19}$$

$$y_f = 1 + \frac{1}{v}\left\{-\phi + \frac{2}{(1 - a_f^2)^{1/2}}\arctan\left[\left(\frac{1 + a_f}{1 - a_f}\right)^{1/2}\tan\frac{\phi}{2}\right]\right\},$$

$$-\frac{\pi}{3} + \delta\phi \le \phi \le 0. \tag{20}$$

Equation (19) may be used for values of a_b of magnitude less than unity. For values of a_b in excess of unity (which can arise for high enough back pressures) an alternative form is more convenient:

$$y_b = 1 + \frac{1}{v}\left\{-\phi + \frac{2}{(a_b^2 - 1)^{1/2}}\operatorname{arctanh}\left[\left(\frac{a_b - 1}{a_b + 1}\right)^{1/2}\tan\frac{\phi}{2}\right]\right\},$$

$$a_b > 1. \tag{21}$$

Negative values of a_b with magnitude $|a_b| > 1$ can also arise under certain circumstances. For such cases,

$$y_b = 1 + \frac{1}{v}\left\{-\phi - \frac{2}{(a_b^2 - 1)^{1/2}}\operatorname{arctanh}\left[\left(\frac{a_b - 1}{a_b + 1}\right)^{1/2}\tan\frac{\phi}{2}\right]\right\},$$

$$|a_b| > 1, \quad a_b < 0. \tag{22}$$

B. Formulating constraint equations

Since all three films must meet at the vertex, we have a constraint

$$y_s(\delta\phi) = y_b\left(\frac{\pi}{3} + \delta\phi\right) = y_f\left(-\frac{\pi}{3} + \delta\phi\right). \tag{23}$$

There is also an integral constraint on the lens area. Using subscripts b and f on integral signs to denote front and back films,

$$A_l = \int_b (1 - y_b)dx_b + \int_f (1 - y_f)dx_f. \tag{24}$$

Parametrizing the back and front films using ϕ,

$$A_l = \int_0^{\pi/3+\delta\phi}(1 - y_b)\frac{dx_b}{d\phi}d\phi + \int_{-\pi/3+\delta\phi}^{0}(1 - y_f)\frac{dx_f}{d\phi}d\phi. \tag{25}$$

Note that it is *essential* to have an area constraint written in this integral form. A constraint saying that the rate of change of lens area vanishes (as is regularly employed in *unsteady*-state viscous froth simulations) is insufficient for this steady-state computation (see Appendix C).

Now Eqs. (12)–(14) are substituted into Eqs. (18)–(21), and thence into constraints (23)–(25), employing also Eq. (11) in Eq. (25). Then, for a given driving back pressure p_b, there are three constraint equations and three unknowns to evaluate: namely, $\delta\phi$ (the turning angle of the spanning film), v (the migration velocity of the structure), and p_l (the pressure of the lens bubble).

These can be solved numerically. Before considering the numerical solutions, however, we analyze a perturbation technique for which solutions for a weakly driven lens may be obtained.

IV. WEAKLY DRIVEN LENS

In the case of a weakly driven lens ($p_b \ll 1$), constraints (23), substituting from Eqs. (18)–(20), need to be expanded perturbatively in powers of the small parameters a_f, a_b, and $\delta\phi$.

This technique of solution is actually quite tedious owing to the nature of Eqs. (16) and (17). When $a_f \to 0$ and $a_b \to 0$ both equations have two terms on their right-hand sides which exactly cancel one another. A first-level expansion of Eqs. (16) and (17) is required merely to detect the equilibrium lens shape, and a next-order expansion is needed to see the perturbation away from equilibrium. Nevertheless, once the expansion is complete, a_f and a_b can be approximated as

$$a_b \approx a_f \approx \frac{v}{p_l^{\circ}}, \tag{26}$$

where p_l° is the equilibrium lens pressure. Then using Eq. (12) to eliminate a_s in Eq. (18) in favor of v, relations can be obtained for v and $\delta\phi$ in terms of the imposed back pressure p_b.

The solutions of these (in the $p_b \ll 1$ limit) turn out to be

$$\delta\phi = \frac{\sqrt{3}}{2}\left(\frac{\left(\frac{4\pi}{3\sqrt{3}} + 1\right)}{2 + \left(\frac{4\pi}{3\sqrt{3}} - 1\right)l} - 1\right)\frac{p_b}{p_l^{\circ}} + O(p_b^3), \tag{27}$$

$$v = \left[1 + \frac{1}{2}\left(\frac{4\pi}{3\sqrt{3}} - 1\right)l\right]^{-1} p_b + O(p_b^3). \tag{28}$$

These same results can be obtained much more simply by expanding Eqs. (16) and (17) in powers of a_b and a_f and then integrating, rather than expanding, the already integrated forms (19) and (20). This provides a robust check on the results.

Note that it is not necessary to know the perturbation to p_l (away from p_l°) in order to find either v or $\delta\phi$. If one wants to know $p_l - p_l^{\circ}$, it is essential to invoke the area constraint equation (25); i.e., the lens area constraint is wholly concerned with fixing the pressure of the lens bubble in the weakly driven limit. This is noteworthy because (as we shall see later) the area constraint concerns itself with fixing different state parameters in a strongly driven lens.

Corrections at order p_b^3 (albeit with an unknown l dependence) have been shown on the right-hand sides of Eqs. (27) and (28). These can be deduced from an elegant symmetry argument as follows. The system is only driven by the *pressure difference* imposed across the spanning film. Thus imposing pressure p_b on one side of that film and nil pressure on the other is equivalent to imposing $\frac{1}{2}p_b$ on one side and $-\frac{1}{2}p_b$ on the other. The only change between the two situations is that the zero of the pressure scale (which is arbitrary) has been shifted by $\frac{1}{2}p_b$. However, in the latter situation with imposed pressures $\pm\frac{1}{2}p_b$, there is an obvious symmetry upon changing the sign of p_b: under this sign change both the vertex rotation direction and propagation direction switch, but the absolute magnitudes of vertex rotation and propagation speed remain the same. Hence $\delta\phi$ and v are odd functions of p_b and any corrections to the leading $O(p_b)$ behavior of Eqs. (27) and (28) must arise at $O(p_b^3)$.

As stated above, we have not specified the l dependence of the $O(p_b^3)$ correction terms. Numerical evidence (see Secs. V B and V C) suggests that the deviation from the leading $O(p_b)$ behavior is weakest when the lens size parameter l is small. Thus the coefficients of the $O(p_b^3)$ correction terms in Eqs. (27) and (28) could well diminish or even vanish in the limit $l \to 0$: see also Sec. VI C 2.

A. Rotation of the spanning film: Weakly driven limit

Now we analyze Eq. (27) in detail. One interesting observation is that it exhibits a maximum over l. Indeed the maximum turning angle $\delta\phi$ can be shown to be realized for a value of l equal to

$$l = l^{max} \equiv \frac{\left(\sqrt{2 + \frac{8\pi}{3\sqrt{3}}} - 2\right)}{\frac{4\pi}{3\sqrt{3}} - 1} \approx 0.43. \tag{29}$$

Note that this corresponds to a maximum over l at fixed p_b. If the maximum were taken at fixed v, it would occur exactly at $l = \frac{1}{2}$. Fixing p_b actually pushes the maximum to smaller l because v is itself a decreasing function of l at given p_b (see Sec. IV B).

In the limits of either very small or very large lenses, Eq. (27) reduces to

$$\delta\phi = \frac{\sqrt{3}}{2}\left(\frac{2\pi}{3\sqrt{3}} - \frac{1}{2}\right)\frac{p_b}{p_l^{\circ}}, \quad l \to 0, \tag{30}$$

$$\delta\phi = \frac{\sqrt{3}}{2}\,\frac{\left(\frac{4\pi}{3\sqrt{3}} - 1\right)}{\left(\frac{4\pi}{3\sqrt{3}} + 1\right)}\,\frac{p_b}{p_l^{\circ}}(1 - l), \quad l \to 1. \tag{31}$$

Consulting also Eq. (4), it can be seen that both very small lenses and very short spanning films (i.e., large lenses) resist bending: they are very stiff. The similarity between these two states only, however, applies in the weakly driven limit. For large driving forces, the small lens will remain stiff, as the back and front films are geometrically constrained to remain short. However, the very large lens has (as we shall see) a much greater degree of compliance when the driving force is large. It has the freedom to move the vertex away from the (bottom) channel wall, extending the spanning film and vastly reducing the bending stiffness.

There is one interesting aspect of the weakly driven small lens case ($l \ll 1$), concerning the distribution of curvature along the spanning film. It might be thought naively that the spanning film would only develop curvature very near the lens itself and be asymptotically flat farther away. This is in fact *not* the case. Using Eqs. (6), (8), (27), and (28) and expanding, the curvature of the spanning film is found to be

$$p_b - v \approx \frac{1}{2}\left(\frac{4\pi}{3\sqrt{3}} - 1\right) l p_b = O(l p_b) \tag{32}$$

at the channel wall and

$$p_b - v + \frac{1}{2} v\,\delta\phi^2 \approx p_b - v + O\left(p_b\left(\frac{p_b}{p_l^{\circ}}\right)^2\right) = p_b - v + O(l^2 p_b^3) \tag{33}$$

at the vertex. Thus curvature is almost *uniform* along the film. It turns out that curvature *can* be confined to small regions of the spanning film when the lens is small, but only for strongly driven lenses, not weakly driven ones. This point will be discussed in more detail later.

B. Migration velocity: Weakly driven limit

The ratio v/p_b given by Eq. (28) can be thought of as an effective mobility of the lens structure [see also the discussion preceding Eqs. (12)–(14)].

Clearly spanning films attached to very small lenses $l \to 0$ propagate essentially with $v \approx p_b$ (i.e., unit mobility) with only a small correction for curvature. In general, smaller lenses give higher mobility than larger ones. This makes sense as the local drag on the structure is less in positions across the channel where there is only one film rather than two.

C. Perturbed lens pressure

In order to compute the perturbation to lens pressure, it is necessary to work with Eq. (25). Given the complexity of the integral in this equation, it is far simpler to Taylor expand Eqs. (16) and (17) [and additionally Eq. (11)], rather than working directly with Eqs. (19) and (20) as integrands in the area constraint. Even so the calculations remain somewhat tedious, and rather than giving a full mathematical derivation, we will discuss the result using physical arguments.

First, there arise from the back and front films so-called *surface terms* reflecting the fact that the ϕ integration range for these films has been perturbed, growing or shrinking by $\pm\delta\phi$ as the vertex rotates. Owing to the high symmetry of the equilibrium lens these surface terms actually cancel at leading order and do not need to be considered further.

Additionally there are perturbations to the integrands in Eq. (25) which need to be integrated over the *original* ϕ range corresponding to each film of the *equilibrium* lens. These perturbations describe how the area contained in the back and front bulges of the lens are affected by shape changes along the film lengths.

An understanding of these effects can be obtained by examining the (magnitude of the) curvature on the back and front films in the weakly driven limit. From Eq. (6),

$$|\kappa_b| = |p_l - p_b| + v_\perp, \quad \kappa_f = p_l - v_\perp. \tag{34}$$

Positive $v_\perp$ produces drag forces which tighten curvature on the back film (reducing the bulge area), but flatten the front film (increasing the bulge area). The high symmetry of the equilibrium lens structure again implies these effects cancel.

Only pressure effects remain. Increases in p_l tighten both curvatures (reducing the bulge areas), but positive p_b reduces the magnitude of the curvature (increasing the bulge area, but acts on the back film only). Invoking area conservation, the net result is somewhat remarkably

$$p_l = p_l^\circ + \frac{p_b}{2} + O(p_b^2), \quad p_b \ll 1; \tag{35}$$

i.e., the pressure in the steady-state lens is increased by half the imposed back pressure.

The reason this equation is remarkable is that $p_l^\circ + \frac{1}{2}p_b$ is also the *instantaneous* pressure which would result if a back pressure p_b were suddenly imposed on an equilibrium lens. In the viscous froth model, the equation for instantaneous pressure can be derived by integrating $v_\perp ds$ around the bubble surface and setting the result to zero in order to conserve area. A relation between pressures and film lengths results [31]: see Eq. (C2) in Appendix C. The instant the back pressure p_b is switched on for an initial equilibrium lens, both film lengths are equal to $\mathcal{L}^\circ$ [see Eq. (3)] and Eq. (C2) reduces to $p_l = p_l^\circ + \frac{1}{2}p_b$.

Returning to the steady-state system, an elegant interpretation of Eq. (35) can be obtained in terms of total film length of the lens. For weakly driven lenses, if individual film lengths $\mathcal{L}_b$ and $\mathcal{L}_f$ are perturbed to $\mathcal{L}^\circ + \delta\mathcal{L}_b$ and $\mathcal{L}^\circ + \delta\mathcal{L}_f$, respectively, and if p_l is perturbed to $p_l^\circ + \delta p_l$, then Eq. (C2) becomes

$$(2\delta p_l - p_b)\mathcal{L}^\circ \approx -p_l^\circ(\delta\mathcal{L}_b + \delta\mathcal{L}_f). \tag{36}$$

It is clear from this equation that it is not necessary for individual steady-state film lengths (i.e., $\mathcal{L}_b$ and $\mathcal{L}_f$) to remain equal to the film lengths $\mathcal{L}^\circ$ for the equilibrium lens if we want Eq. (35) to apply. It is only required that the *sum* of film lengths remain constant; i.e., elongation of the back film is compensated by shortening of the front film at leading order.

A symmetry argument the same as that in the discussion following Eqs. (27) and (28) can also be invoked here. If pressures $\pm\frac{1}{2}p_b$ are applied, respectively, behind and in front of the spanning film, it is clear on symmetry grounds that the lens pressure must be an even function of p_b. The case we have actually considered, with pressure p_b behind the spanning film and nil pressure in front of it, is identical except for resetting the zero of the pressure scale; i.e., in our case $p_l - \frac{1}{2}p_b$ will be an even function of p_b. For small back pressures, it then follows that $p_l - \frac{1}{2}p_b = p_l^\circ + O(p_b^2)$ in agreement with Eq. (35). Since the symmetry argument can be applied not only at steady state, but also for the unsteady evolution from the initial equilibrium up to final steady state, Eq. (35) actually applies at all times.

D. Perturbed vertex position

In addition to studying film lengths on the lens bubble, it is interesting to know whether the vertex displaces toward one or other wall of the channel. This is particularly crucial for a very short spanning film, since a displacement in the "wrong" direction (shortening that film still further) could signal a transition to a so-called "bamboo" structure [40] in which the lens bubble occupies the entire channel width.

Mathematically the cross-channel displacement is easiest to obtain by expanding front film equation (17) in powers of p_b/p_l° and v/p_l° using Eqs. (14), (28), and (35) and then integrating the perturbation from $-\frac{\pi}{3}$ to 0. A surface term is subsequently subtracted off (recognizing that the true lower limit of the integration domain has shifted to $-\frac{\pi}{3} + \delta\phi$), Eq. (27) is used, and finally the cross-channel vertex displacement is obtained.

Remarkably, at leading order, the weakly driven lens is found to displace neither up nor down: all terms cancel. We have obtained an independent check on the calculation by working with the expansion of back film equation (16) in place of Eq. (17): the same result is obtained. This is also predicted via the symmetry arguments mentioned earlier in connection with Eqs. (27) and (28) and in Sec. IV C: cross-channel vertex displacement should be an even function of p_b, and so has corrections at $O(p_b^2)$ only. A further implication is that the spanning film curves away from its unperturbed position, but does not experience any shortening or lengthening at first order in p_b.

Thus unfortunately no conclusion can be drawn regarding possible bamboo transitions in the $l \rightarrow 1$ limit based on the weakly driven perturbation theory alone. A numerical analysis is required for higher back pressures, and this reveals that the vertex displaces so as to lengthen the spanning film; i.e., no bamboo transition occurs. Indeed the lengthening spanning film increases the compliance of the lens structure, lead-

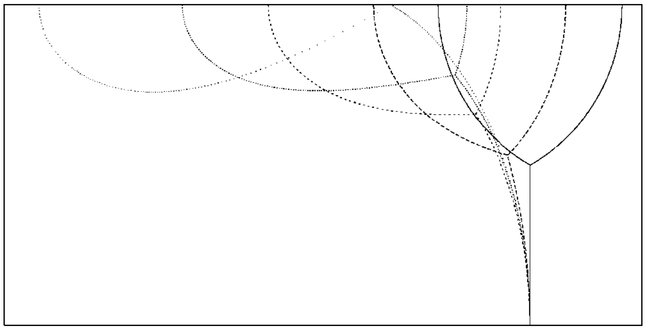

FIG. 4. Steady-state lens structures for a medium-size lens with $l=0.5$ and various back pressures driving the system towards the right: equilibrium lens $p_b=0$ (solid line), $p_b=2$ (long-dashed line), $p_b=4$ (short-dashed line), the end of the original steady-solution branch $p_b\approx 4.64$ (denser dotted line), and a lens on the point of detachment, with $p_b\approx 3.40$ on a new solution branch (fainter dotted line).

ing to further distortion over a comparatively modest range of back pressures. The results of the numerical study are described in the following sections.

V. ACCESSING THE STRONGLY DRIVEN LENS

In this section, we present the steady state (numerical) results of the strongly driven lens as follows. First, we examine some deformed lens structures in detail, and then we go on to describe a key geometrical features of these structures (namely, the cross-channel coordinate of the vertex, denoted y_v, and the spanning-film turning angle $\delta\phi$) parametrically in terms of the driving pressure p_b and lens size parameter l. We then proceed to consider kinematic (migration velocity v) and dynamic (pressure in the lens bubble p_l) properties of the system in terms of these same parameters. Finally a key rheological property—namely, surface energy—is treated: this is of course just equal to total film length in our units, and so is easily related back to the geometry of the structure.

Details of the numerical method employed are given in Appendix D. Briefly the method was an iterative one. It started by using the weakly driven lens theory of Sec. IV as an approximate solution for low back pressure p_b values and then increased p_b in small increments, using the solution at one back pressure as an initial guess for the next.

A. Deformed lens structures (including vertex location)

We consider in Fig. 4 some steady-state structures for a medium-size lens bubble with $l=0.5$ (remember l is the fraction of the channel width occupied by the equivalent area lens at equilibrium). It is clear that as the imposed back pressure p_b grows, the vertex at which the three films meet displaces upwards: Figure 5 shows the vertex vertical coordinate (which we denote y_v) as a function of p_b. The back film and spanning film both lengthen, but the front film actually shortens as the vertex tends to displace along it. This behavior which we have examined here for $l=0.5$ is typical of other lens sizes also, although the departure from equilibrium tends to be weaker when l is small: see also Fig. 5.

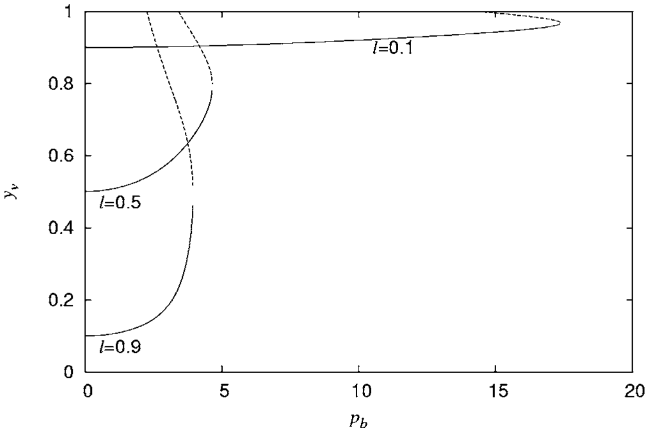

FIG. 5. The vertical vertex position (denoted y_v) across the channel as a function of the back pressure p_b for small ($l=0.1$), medium-size ($l=0.5$), and large ($l=0.9$) lenses. Solid lines indicate the original branch of steady solutions (the vertex displaces upwards as p_b grows along this branch), while dashed lines (with higher y_v values) indicate a new steady-solution branch (y_v displaces downwards as p_b grows): the latter branch is believed unstable: see, e.g., the discussion in Sec. VII B.

B. Rotation of the spanning film

The overall rotation or turning angle along the spanning film $\delta\phi$ is one way of characterising the departure from equilibrium of a driven lens structure.

In Fig. 6 we compute this as a function of p_b for three different lens bubble sizes: a small lens $l=0.1$, a medium-size lens $l=0.5$, and a large lens $l=0.9$. Also shown in Fig. 6 are the weakly driven perturbation formulas from Eq. (27) for $l=0.1$, $l=0.5$, and $l=0.9$.

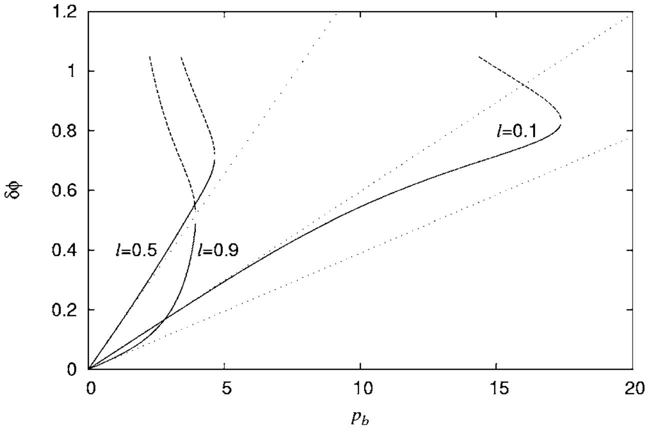

FIG. 6. The steady-state turning angle along the spanning film $\delta\phi$ as a function of back pressure p_b for small ($l=0.1$), medium-size ($l=0.5$), and large ($l=0.9$) lenses. Solid lines indicate the original branch of steady solutions, while dashed lines (with higher $\delta\phi$ values) indicate a new steady-solution branch: the latter branch is believed unstable. The dotted lines indicate the asymptotic formula for the weakly driven lens for each l value.

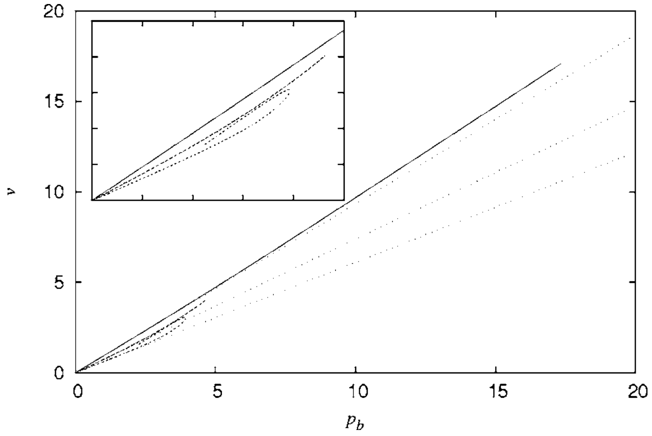

FIG. 7. The steady-state migration velocity v of the lens structure as a function of back pressure p_b. Solid line: $l=0.1$. Long-dashed line: $l=0.5$. Short-dashed line: $l=0.9$. For the $l=0.9$ data both the original steady-solution branch (lower part of the short-dashed curve) and the new branch (upper part of the short-dashed curve which loops backward) are shown. Only the original branch is shown for other l values, as the branches virtually overlie each other in these cases. For clarity the inset shows a close-up view of the region $0 \leq p_b \leq 5$, $0 \leq v \leq 5$. Returning to the main plot, the asymptotics for the weakly driven lens are also shown (dotted lines, one for each l value), giving velocity values slightly less than the computed ones. In all cases, however, the computed velocities satisfy $v < p_b$.

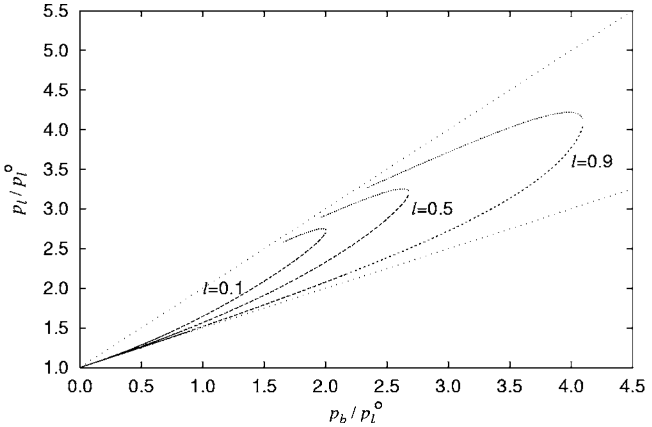

FIG. 8. The steady-state pressure of the lens bubble p_l normalized by equilibrium pressure p_l° as a function of (normalized) back pressure p_b/p_l°. Various lens sizes are shown, $l=0.1$, $l=0.5$, and $l=0.9$. On the original solution branch, solid lines show regions where $p_l > p_b + v$ [as a result the film mobility parameter a_b defined by Eq. (13) satisfies $0 < a_b < 1$]. Long-dashed lines show regions where $p_b < p_l < p_b + v$ (as a result $a_b > 1$). The short-dashed line (which only applies for $l=0.9$) shows regions where $p_b > p_l$ (and hence a_b is negative). The dense dotted lines show the new solution branch (Sec. VI D). The faint dotted lines show $p_l = p_l^{\circ} + \frac{1}{2} p_b$ (which is the asymptotic behavior for a weakly driven lens) and $p_l = p_l^{\circ} + p_b$. All data values lie between these two limits.

For $p_b \ll 1$, the results for $l=0.1$ and $l=0.9$ are similar, as Eqs. (30) and (31) predict, while $l=0.5$ exhibits close to maximal rotation [being relatively near $l^{max} \approx 0.43$; see Eq. (29)].

As p_b increases, $\delta\phi$ for the $l=0.1$ system remains close to the linear perturbation formula, while data for $l=0.5$ and $l=0.9$ are superlinear in back pressure. Moreover, growth in $\delta\phi$ for $l=0.9$ becomes so rapid that it eventually approaches the $l=0.5$ case.

Note that we have been unable to obtain steady solutions beyond a certain critical back pressure (which depends on l). Immediately before this pressure, both y_v (Fig. 5) and $\delta\phi$ (Fig. 6) show an especially rapid increase. We shall analyze the nature of this critical back pressure in Sec. VI: for the present, however, we just treat it as a restriction on the available solution domain. Small l values tend to lead to high critical back pressures and hence wide solution domains.

C. Migration velocity

Values of the migration velocity v for the parameter values ($l=0.1$, $l=0.5$, and $l=0.9$) considered earlier are shown in Fig. 7. Perturbation formulas from Eq. (28) are also shown. Clearly small lenses move faster than large ones.

The linear perturbation laws do not perform too poorly, but superlinear growth is detectable especially for the medium size $l=0.5$ and large lenses $l=0.9$, which migrate towards the $l=0.1$ data. This is believed to be associated with the vertex shifting upwards towards the top of the channel (effectively replacing two films by a single one over part of the channel width) and also with the lens bubble reorienting its films as it becomes squashed against the channel wall [film segments oriented tangential to the direction of motion exhibit no drag in the viscous froth model: this is in line with experimental observations that only the projected lengths of films normal to the direction of migration are needed to determine the drag [36] and also with theoretical results (for bubble motion in capillaries) showing the ease and rapidity with which liquid held between films and confining container walls can be transported in the case where films are oriented along a bubble migration direction [41,42]].

Note that despite this tendency to squash the lens bubble somewhat, it is never possible for this bubble to become *arbitrarily* long and thin in a steady-state migrating structure. We argue this by contradiction: if the lens bubble were a long thin structure along the channel wall, the back film would have to be flat and parallel to the wall for most of its length. Since curvature κ and normal velocity $v_\perp$ would both vanish on any flat, parallel region, Eq. (6) implies that no pressure difference could be sustained across the back film—i.e., $p_l = p_b$. Both the front film and the spanning film would have to turn through $\frac{\pi}{6}$ angles in order to join up with the flat section of the back film at the correct angle. However, with $p_l = p_b$ these two films require equal distances across the channel to turn through equal angles: this is contradictory as it locates the three film meeting point in the middle of the channel instead of near one wall.

D. Lens pressure

Figure 8 plots the values of the steady-state lens pressure. We have normalized both p_l and p_b by equilibrium pressure

p_l° so as to collapse data from different l values together. It is clear that

$$p_l^\circ + \frac{p_b}{2} < p_l < p_l^\circ + p_b. \tag{37}$$

If p_b is small, then p_l values cluster around the lower end of this inequality range [as Eq. (35) predicts]. However, as p_b grows, p_l migrates towards the upper end of the range.

Note that it is not essential that $p_l > p_b$, and indeed this condition tends to be violated for large lenses over a moderate p_b range. In order to achieve $p_l < p_b$, but still satisfy inequality (37), p_l° needs to be a moderately small fraction of p_b [which, by Eq. (4), is easiest to achieve for large l] and p_l cannot have migrated too close to $p_l^\circ + p_b$.

For large lenses, there exist special parameter choices, for which $p_l = p_b$: the back film then propagates at a constant migration velocity through purely curvature driven growth. Such curvature driven growth solutions are well known in the literature [30,43], where they are called "Mullins finger" or "grim reaper" solutions. In other words, the back film is, under special circumstances, just a segment of a Mullins finger. Our back films are necessarily segments of a Mullins finger that turn through less than $\frac{\pi}{2}$; otherwise, the contradiction discussed in Sec. V C comes into play.

There is a noteworthy computational consequence of the above observations concerning lens pressure. For weakly driven lenses, $p_l \approx p_l^\circ$, $p_b \ll p_l$, and $v \ll p_l$. As p_b increases, it is possible (depending on lens size) that p_b becomes as large as p_l. Before this happens, however, there is necessarily a p_b value for which $p_l = p_b + v$. The back film mobility parameter a_b defined in Eq. (13) passes through the value unity as this point: a switch from computing film position via Eq. (19) to Eq. (21) then occurs. Subsequently, when and if p_b reaches the value p_l, the film mobility parameter becomes infinite: the film propagates through curvature alone, with no driving pressure force. In the region where p_b exceeds p_l the mobility parameter is negative: the film migrates forward due to curvature despite an adverse pressure difference across it. Equation (21) remains well defined in spite of this behavior of a_b.

E. Lens energy

The lens surface energy can be obtained by integrating Eq. (9) for each film. Recalling the definition of the various mobility parameters a_s, a_b, and a_f from Eqs. (12)–(14) and following an integration procedure analogous to that used to obtain Eqs. (18)–(22) from Eqs. (15)–(17), we find the film lengths $\mathcal{L}_s$, $\mathcal{L}_b$, and $\mathcal{L}_f$, respectively, for the spanning, back and front films,

$$\mathcal{L}_s = \frac{a_s}{v}\frac{2}{(1-a_s^2)^{1/2}} \arctan\left[\left(\frac{1+a_s}{1-a_s}\right)^{1/2} \tan\frac{\delta\phi}{2}\right], \tag{38}$$

$$\mathcal{L}_b = \frac{a_b}{v}\frac{2}{(1-a_b^2)^{1/2}} \arctan\left[\left(\frac{1-a_b}{1+a_b}\right)^{1/2} \tan\frac{(\delta\phi+\pi/3)}{2}\right],$$

$$|a_b| < 1, \tag{39}$$

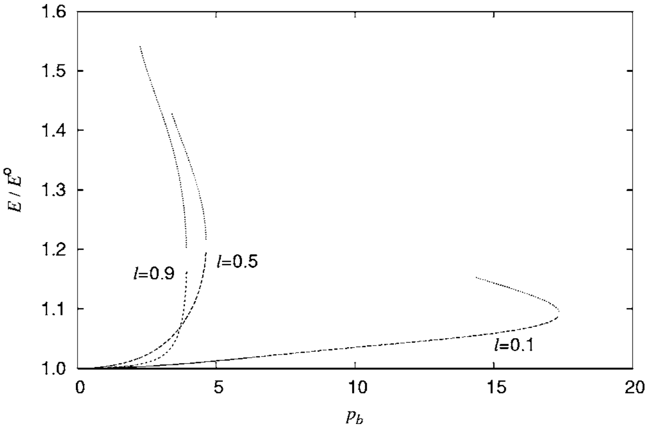

FIG. 9. The surface energy of the lens structure (denoted E) normalized by the equilibrium energy E° as a function of back pressure p_b for various lens sizes l. Only a second-order increase in energy is seen for small p_b. On the original solution branch, the solid lines indicate regions where the back film mobility parameter a_b satisfies $0 < a_b < 1$, the long-dashed lines indicate regions where $a_b > 1$, and the short-dashed line (in the case of $l = 0.9$) regions where a_b is negative. Meanwhile, the dotted lines show the new solution branch (see Sec. VI D), which is of higher energy and believed unstable.

$$\mathcal{L}_f = \frac{a_f}{v}\frac{2}{(1-a_f^2)^{1/2}} \arctan\left[\left(\frac{1+a_f}{1-a_f}\right)^{1/2} \tan\frac{(\pi/3-\delta\phi)}{2}\right]. \tag{40}$$

Equation (39) applies for $|a_b| < 1$. In the case where $|a_b| > 1$, for the back film

$$\mathcal{L}_b = \frac{2}{v(1-a_b^{-2})^{1/2}} \operatorname{arctanh}\left[\left(\frac{a_b-1}{a_b+1}\right)^{1/2} \tan\frac{(\delta\phi+\pi/3)}{2}\right],$$

$$|a_b| > 1. \tag{41}$$

The three film lengths are summed to obtain the total surface energy $E = \mathcal{L}_s + \mathcal{L}_b + \mathcal{L}_f$, and the energy is then normalized by the equilibrium energy E°; see Eq. (5). The result is shown in Fig. 9. For small back pressures, there are only weak (i.e., second-order) increases in energy. This is consistent with results in Secs. IV C and IV D which show that neither the spanning film length nor the sum of the back and front film lengths change at first order in p_b. Indeed the overall film energy is, on symmetry grounds, necessarily an even function of p_b: thus only $O(p_b^2)$ perturbations to E° are permitted for small p_b. However, larger energy increases are seen as p_b grows, particularly for moderate $l = 0.5$ and large $l = 0.9$ lenses. The increase in energy is particularly rapid around the critical pressure (mentioned also in Sec. V B) where steady solutions break down.

VI. BREAKDOWN OF STEADY SOLUTIONS

By stepping upwards in back pressure in extremely small increments (5×10^{-4}), we have determined the critical pressure and the corresponding migration velocity at which steady solutions break down as functions of the lens size

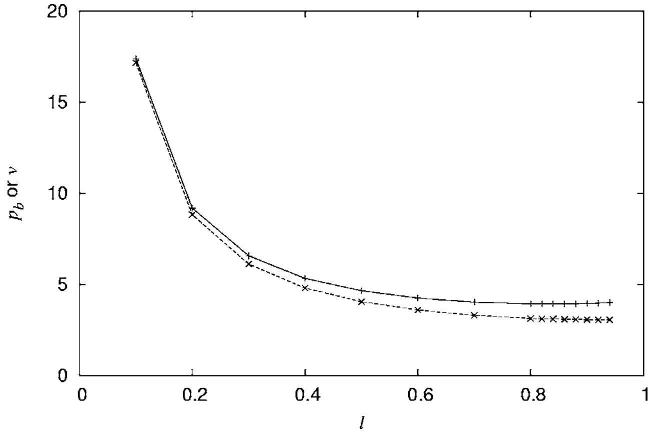

FIG. 10. The (critical) pressure p_b (solid line with +) and velocity v (dashed line with ×) at which steady solutions break down as functions of the lens size parameter l.

parameter l: the results are plotted in Fig. 10. The migration velocity v at breakdown is a decreasing function of l. Meanwhile, the critical pressure p_b is likewise a decreasing function for most l values, but starts to increase very slightly after about $l=0.82$: this slight increase (which in relative terms is only on the order of a few percent) is consistent with larger lenses having more overall length of film and hence lesser mobility (v/p_b) than smaller ones.

The fact that the front film seems to shrink in length as the back pressure grows from zero to the critical value (cf. Sec. V A) suggests one of two possibilities. These are that (i) the steady-state length of the front film shrinks continuously to zero, becoming vanishingly short at the critical back pressure, or (ii) the structure loses stability even while the front film length is still finite.

We first discuss the physical implications of the two different possibilities, then the procedure we employed to distinguish between them, and subsequently what has been learned from this procedure. The outcome of this analysis is that the latter possibility—i.e., loss of stability—appears to be the one realized in practice.

A. Continuous decrease of film length vs loss of stability

For a continuous decrease of the steady-state front film length to zero to apply, quasistatic increments in the back pressure would lead to quasistatic decreases in the front film length and arbitrarily short front films could be accessed quasistatically. Once the critical back pressure is exceeded, the system would undergo a topological transformation (see Fig. 11): the lens bubble and the spanning film would detach. The spanning film would now cross the entire channel and (given the model associates no drag to film end points) would propagate forward as a flat film with velocity $v=p_b$. The former lens bubble of area A_l would relax to a semicircular shape, with a curvature radius $(2A_l/\pi)^{1/2}$ and hence a pressure $p_l=p_b+(2A_l/\pi)^{-1/2}$, and would not propagate. Such semicircular bubbles attached to channel walls have been observed in two-dimensional foam channel flow experiments [44]. Once formed, they are difficult to flush out of the channel: if the back pressure p_b is increased, they stay fixed in position and merely increase their own internal pressure p_l by an equivalent amount.

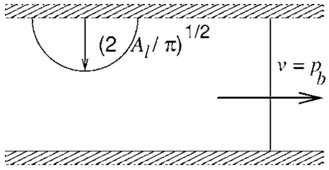

FIG. 11. The breakdown of the lens structure following a topological transformation. The former spanning film is flat and propagates with velocity equal to back pressure $v=p_b$. The former lens bubble (area A_l) remains behind and is semicircular in shape with radius $(2A_l/\pi)^{1/2}$, the relation between A_l and the lens size parameter l being given by Eq. (2).

For the alternative scenario of steady solution breakdown (i.e., loss of stability), once the critical back pressure is exceeded, it is *still* possible that the above-mentioned topological transformation takes place. However, approaching it now becomes an inherently *dynamic* phenomenon: it is not possible to maintain arbitrarily short front films for indefinite time periods by suitably fixing the back pressure.

Loss of stability at finite film size has been observed in other foam systems subject to deformation. For instance, a regular three-dimensional foam structure, known as the Kelvin foam, has been studied under slow extension and/or shear [13,14]. As the shear proceeds, certain films shrink and others grow: the actual structure of the foam can be computed by minimizing the surface energy of the structure subject to boundary conditions imposed by the shear. Beyond a critical shear strain, however, there is no longer an energy minimum even though all films are of finite size. The configuration that corresponds to a stationary point of the surface energy switches from being an energy minimum to a saddle. The system can run away to a topological transformation with no additional increment in strain. Similar behavior has also been observed with other regular three-dimensional foam structures under strain [16].

Another example is dilation of a foam staircase structure in a cylindrical tube [40]. There are flat film faces attached normal to the cylinder wall that partly fill the cross section and alternate across the cylinder. Additionally there are films that zigzag across the cylinder like stairs, and these join up the flat films. As the structure is dilated quasistatically, the relative size of the flat films and zigzag films changes: the actual structure is computed by energy minimization. Beyond a certain dilation, even though all films are of finite size, the energy switches from having a minimum to a saddle. A runaway to a topological transformation, leading in this case to a bamboo structure, then ensues.

The loss of stability that we postulate is reminiscent of the examples just discussed, but with one important difference. We are no longer dealing with a quasistatic applied strain for which energy minimization can be applied to determine structure; instead we are considering the steady state of an out-of-equilibrium foam (even though the back pressure that determines the amount of departure from equilibrium may itself be varied quasistatically). If the structure is deformed somehow away from the steady state at any given back pressure, there will be a set of eigenmodes and eigenvalues governing the rate to return (or otherwise) to that state. If the eigenvalue corresponding to the least stable mode reaches zero at some critical back pressure, this signals a loss of stability.

B. Lens on the point of detachment

The methodology we have employed for determining the nature of the breakdown of steady solutions is as follows. We consider a steady-state lens with a vanishingly small front film; i.e., the lens bubble is on the point of detaching from the spanning film. We try to determine the conditions (and in particular the back pressure) under which such a structure could exist. If the back pressure we compute corresponds to the value already observed where the steady solution branch breaks down, this points to continuous shrinkage of the front film length to zero. If the back pressure we compute has some other different value, loss of stability at the critical back pressure is implied.

The latter possibility is in fact what we observe. The back pressure required to propagate the lens on the point of detachment is actually *lower* than the critical pressure corresponding to a breakdown of steady solutions. The lens on the point of detachment is not even on the original steady-solution branch, but is in fact the starting point of a new steady-solution branch (believed unstable for reasons to be discussed in Sec. VII B). The new solution branch can be followed from its starting point up to higher pressures, but like the original branch, also terminates at the critical back pressure.

In order to have a lens on the point of detachment, it is necessary that the back film turn through an angle $\frac{2\pi}{3}$ along its length, returning to the top of the channel at this point. This allows it to meet, at the correct angle, an arbitrarily short front film that is flat and oriented normal to the top channel wall.

We need to find out whether either Eq. (19) or (21) can have a solution with $y_b=1$ when $\phi=\frac{2\pi}{3}$. It turns out that Eq. (19) has no such solution, but Eq. (21) admits a solution when

$$a_b \equiv v/(p_l - p_b) \approx 1.756. \tag{42}$$

The area constraint [Eq. (25)] can now be invoked: the integral over the back film runs from $\phi=0$ through $\phi=\frac{2\pi}{3}$. It is clear from Eqs. (11), (13), and (21) that $1-y_b$ and $dx_b/d\phi$ appearing in the integrand of Eq. (25) can be written in terms of shape functions (depending only on the known a_b and on ϕ) and an overall scale factor v^{-1}. In other words, any lens on the point of detachment has a given shape, regardless of size. Invoking the area constraint only fixes the propagation velocity (contrast this situation with weakly driven lenses, Sec. IV, for which the area constraint was wholly concerned with setting the pressure of the lens bubble). After performing a quadrature on the shape functions,

$$v \approx 1.276 A_l^{-1/2} \approx 1.410 l^{-1}, \tag{43}$$

where Eq. (2) has also been used.

Thus small lens bubbles have to move very quickly before they are on the point of detachment, but larger lens bubbles can achieve this state for modest propagation velocities. To date we have computed the velocity with which a nearly detached lens of a given size will propagate: we have not yet determined the back pressure corresponding to detachment. This issue is addressed in the next subsection.

C. Propagation of the spanning film

In order to find the back pressure p_b corresponding to a nearly detached lens, it is necessary to analyze the spanning film. The analysis we shall present will correspond not only to the case of a spanning film with a nearly detached lens bubble of arbitrary size, but also to *any* fast-moving lens structure, with a small lens bubble, whether near the point of detachment or not. The reason for the close correspondence between these two situations is obvious: in both cases the spanning film is required to span virtually the entire channel; i.e., the cross-channel coordinate of the vertex, denoted y_v, is near unity.

For a nearly detached bubble the spanning film is required to rotate through an angle $\delta\phi=\frac{\pi}{3}$ by the position $y_v=1$. Since the velocity v corresponding to near detachment is known by Eq. (43), then Eq. (18) gives a relation for $a_s=v/p_b$ and hence p_b. A Newton-Raphson technique [45] can be used to find p_b. Convergence of the Newton-Raphson method can be guaranteed by starting with small lens bubbles, for which values of a_s near unity should apply, and then moving to progressively larger lens bubbles. The relation between back pressure and velocity thus obtained is shown in Fig. 12.

D. Fast-moving small lenses

Small lens bubbles on the point of detachment necessarily propagate quickly [Eq. (43)]. In fact an asymptotic relation between back pressure and propagation velocity can be obtained for *any* fast-moving lens structure with a small lens bubble.

This is derived as follows. If a_s is near unity and the turning angle ϕ at some arbitrary point on the spanning film is not too small (in a sense to be made precise shortly), then the arctan term in Eq. (18) evaluates to $\frac{\pi}{2}$. Again, as a_s is near unity, the $-\phi$ term on the right-hand side of Eq. (18) is negligible and after some rearrangement we deduce

$$p_b \approx \left(1 + \frac{\pi^2}{2v^2}\right) v, \quad l \ll 1,\ v \to \infty, \tag{44}$$

$$v \approx \left(1 - \frac{\pi^2}{2p_b^2}\right) p_b, \quad l \ll 1,\ p_b \to \infty, \tag{45}$$

$$a_s \approx \left(1 - \frac{\pi^2}{2p_b^2}\right), \quad l \ll 1,\ p_b \to \infty. \tag{46}$$

The asymptotic formula (45) is shown in Fig. 12. It agrees well with the true lens velocity for fast-moving, nearly detached lens structures—i.e., small lens bubbles.

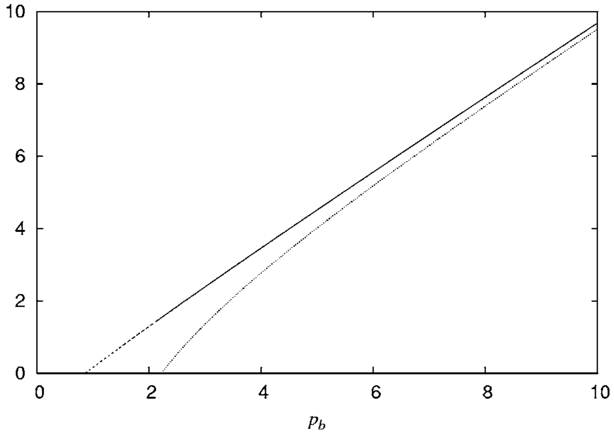

FIG. 12. The velocity of a lens on the point of detachment as a function of the back pressure corresponding to detachment (solid line). The long-dashed extension of the line towards lower back pressures and velocities corresponds to parameter values which cannot be realized starting from an equilibrium lens (regardless of the stability or otherwise of the nearly detached lens structure), because the resulting nearly detached lens would have an area greater than an equilibrium lens with $l=1$. The short-dashed extension towards even lower back pressures and velocities corresponds to parameter values that cannot be realized for any lens structure as the nearly detached lens bubble itself would span more than one channel width. The zero-velocity point corresponds to a back pressure for which the spanning film is a circular arc subtending $\frac{\pi}{3}$. The approximate velocity formula, Eq. (45) (dotted line), asymptotes to the data for large back pressure.

Note that the analysis we have used to deduce Eqs. (44) and (45) has not assumed any particular turning angle $\delta\phi$ at the end of the spanning film: merely that this angle be "not too small." Hence it is not restricted to the particular case of a nearly detached lens with $\delta\phi=\frac{\pi}{3}$. As stated earlier, any fast-moving small lens bubble can be considered. Moreover, owing to the nature of the arctan function, a broad range of ϕ values all map to the same y_s value at or near the top of the channel. Specifically any ϕ value greater than order $(1-a_s)^{1/2}\approx\pi/(\sqrt{2}p_b)$ lies at the top of the channel; i.e., $d\phi/dy$ is exceedingly large there.

This is a very clear indication that curvature [which by Eqs. (7), (9), and (10) is simply $\cos\phi\, d\phi/dy$] is confined in a boundary layer near the top of the spanning film: curvature confined to boundary layers has previously been observed in other foam systems, such as a staircase foam in a cylindrical tube [40]. This boundary layer picture is, however, a very different situation from the slowly driven lens structure with a small lens bubble, for which curvature is more or less uniformly distributed along the spanning film [see Eqs. (32) and (33)].

E. Slow- vs fast-moving small lenses

It is desired to reconcile the small lens bubble theories ($l\ll1$) in the low- and high-p_b limits and specifically to identify the range of p_b values for which the transition between the two theories is realized.

From Eq. (28) we have the following weak back pressure analogs of Eqs. (45) and (46):

$$v\approx\left[1-\frac{1}{2}\left(\frac{4\pi}{3\sqrt{3}}-1\right)l\right]p_b,\quad l\ll1,\ p_b\to0,\tag{47}$$

$$a_s\approx\left[1-\frac{1}{2}\left(\frac{4\pi}{3\sqrt{3}}-1\right)l\right],\quad l\ll1,\ p_b\to0.\tag{48}$$

For the low-p_b limit to apply, it is necessary that at the top of the spanning film both the tan and arctan terms in Eq. (18) be replaced by their arguments. For the tan term it is sufficient to have $p_b/p_l^\circ\ll1$ [see Eq. (30)], but the requirement for the arctan term is more stringent. Since $1-a_s$ is $O(l)$ by Eq. (48) and p_b° is $O(l^{-1})$ by Eq. (4), we deduce the transition between slow-moving (the argument of the arctan is small) and fast-moving (the argument of the arctan is large) theories when

$$p_b\sim O(l^{-1/2}),\quad l\ll1.\tag{49}$$

Evidently, with small l, the range of validity of the weakly driven lens theory is quite wide, a fact we have already observed in Sec. V B.

A universal form for the small l theory can now be proposed:

$$v\approx[1-lF(p_b^2l)]p_b,\quad l\ll1,\tag{50}$$

where F is a function of p_b^2l, with the properties that $F\to\frac{1}{2}(\frac{4\pi}{3\sqrt{3}}-1)$ as $p_b^2l\to0$ and $F\sim\frac{\pi^2}{2}(p_b^2l)^{-1}$ as $p_b^2l\to\infty$. In particular, assuming the function F is smooth and considering a correction to the leading-order slow-moving behavior, the coefficient of the generic $O(p_b^3)$ correction term in Eq. (28) would itself be multiplied by an $O(l^2)$ coefficient in the $l\ll1$ limit.

F. A new branch of steady solutions

The data in Fig. 12 along with Eq. (43) can be used to determine a relation between the detachment back pressure p_b and the lens size l. In all cases where we have observed steady solutions ceasing to exist at some critical back pressure, the back pressure corresponding to a lens on the point of detachment is *less* than the critical one. Moreover, if we follow the original solution branch up to the critical pressure, the value of $\delta\phi$ (the rotation of the spanning film) is always considerably less than $\frac{\pi}{3}$ (the value that corresponds to a lens on the point of detachment). Thus the lens on the point of detachment is not the end point of the original solution branch: rather it is on a new branch altogether.

We can follow this branch using the same technique we used to track the original solution branch. Given a lens size l, we know the pressure p_b corresponding to detachment. We also know the velocity v, the spanning film rotation $\delta\phi$, and the lens pressure p_l [obtained from Eqs. (13) and (42)]. We can then perturb p_b slightly and determine how v, $\delta\phi$, and p_l vary to maintain constraints (23)–(25). Solutions are available for *increasing* values of p_b from that of the nearly detached lens up to the critical back pressure, corresponding to the disappearance of steady solutions. It is clear from Fig. 6,

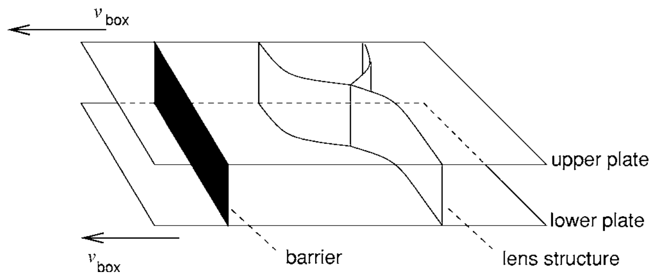

FIG. 13. The sliding matchbox system. A foam (e.g., the lens structure) is confined between glass plates that slide over an impenetrable barrier. As drawn, the plates move to the left at speed v_{box} relative to some laboratory frame, while the barrier and the lens structure (if and when it reaches steady state) do not move in the laboratory frame.

which shows the spanning film turning angle $\delta\phi$, that these two branches meet, after which point the steady solutions disappear.

The mathematical behavior of the equations near the critical back pressure can be analyzed by computing the Jacobian of the constraint violations (at a specified back pressure) with respect to v, $\delta\phi$, and p_l. This Jacobian becomes singular, indicating that there is a particular direction (in the vector space of v, $\delta\phi$, and p_l) for which no leading-order constraint violation occurs: it is this property that generates the two solution branches.

VII. UNSTEADY-STATE BEHAVIOR OF THE LENS

In the previous section, we determined that there appear to be two branches of steady solutions for the lens structure. One joins up continuously with the equilibrium (and weakly driven) lens, the rotation of the spanning film $\delta\phi$ being an increasing function of driving pressure p_b. The other branch appears at finite p_b and has high $\delta\phi$ values, which, however, *decrease* as p_b increases. The branches meet (and steady solutions disappear) at a certain critical driving pressure, the value of the critical pressure depending on the lens size.

Only an unsteady-state analysis can answer definitively the question as to which of the two branches is stable. Moreover, the unsteady-state analysis can also address the issue of what happens to the structure if the critical back pressure is exceeded. The algorithms used to implement the unsteady-state analysis are discussed in detail in Appendix E. In the present section, we concentrate just on the physical description and results of that analysis.

A. Physical description of unsteady-state lens: The sliding matchbox foam

The physical problem we consider is a foam confined between glass plates where the plates are moved with respect to some laboratory frame. An impenetrable barrier spans the gap between the plates, and this barrier is fixed in the laboratory frame. We call this system (see Fig. 13) a *sliding matchbox foam* as the plates slide over the barrier in much the same way as the cover of an opening matchbox slides over the box within. We suppose that the plate motion is to the left at speed v_{box}; i.e., the plate velocity relative to the laboratory frame is $-v_{box}\boldsymbol{e}_x$, where $\boldsymbol{e}_x$ denotes a unit vector along the direction of sliding.

The viscous froth lens is initially in its equilibrium configuration and is some distance in front of the impenetrable barrier. Under the action of the sliding plates the lens reconfigures itself, subject to the constraint that the area between the barrier and the back of the lens structure remains fixed.

This sliding matchbox problem is actually entirely analogous to one in which the plates are fixed but the volume of the back bubble behind the plates grows in area at a constant rate $\dot{A}_b$. The proof of this is given in Appendix E 4 c. Since the channel has unit dimensionless width, the analogy requires v_{box} for the sliding matchbox problem to be equated to $\dot{A}_b$ for the system with a growing back bubble.

In the sliding matchbox problem, the control variable determining the ultimate fate of the system is the plate speed v_{box} relative to the laboratory frame. This differs slightly from our steady state computations in Secs. III–VI where the back pressure p_b was treated as the control variable and the apparent propagation speed v of the foam lens structure relative to the plates was a response variable. If a steady state exists for the sliding matchbox system, v_{box} (the sliding box speed relative to the laboratory) and v (the speed of the lens structure relative to the box) must be opposite and equal. Thus the steady-state sliding matchbox foam structure is fixed in the laboratory frame. Before steady state is reached, however, different elements of film propagate at different apparent velocities. On the approach to steady state, the back pressure p_b will now vary with time, but once steady state is achieved, we will obtain solutions identical to those discussed in Secs. III–VI. Thus questions regarding stability of those steady solutions can still be addressed.

B. Relaxation to steady state

The first set of unsteady state simulations that we considered started with an equilibrium lens structure, which was suddenly set into motion via some plate sliding velocity v_{box}. Values of v_{box} were chosen to be in the range for which steadily migrating solutions with v canceling v_{box} are known to be possible.

In all cases that we examined (various l and v_{box} values) solutions settled over time into a steady state corresponding to the *original* branch of steady solutions—i.e., the branch joining up continuously with the equilibrium $p_b=0$ state: we conclude that this branch is the stable one.

The alternative steady-solution branch (identified in Sec. VI D) has not been observed as the final state of any unsteady simulations, at least not in cases where the initial condition is the equilibrium lens structure. This supports our belief that the branch in question is unstable. This is, moreover, consistent with general bifurcation theory [46]: steady-state solutions should appear (or in this particular case disappear) in a stable-unstable solution pair at a so-called saddle-node bifurcation. The fact that the branch should be unstable helps to reconcile some of its counterintuitive physical properties: e.g., vertex rotation $\delta\phi$ (Fig. 6) and sur-

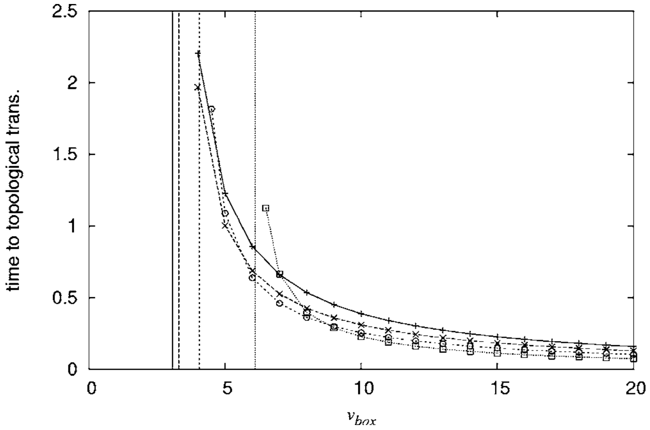

FIG. 14. Dimensionless time for the occurrence of the topological transformation (lens bubble detaching from the spanning film) as a function of the driving velocity v_{box} for rapidly driven systems that have no steady state. The initial condition upon start up of the driving velocity was the equilibrium lens structure. Various lens sizes are shown: Solid line with $+$:l=0.9. Long-dashed line with $\times$:l=0.7. Short-dashed line with $\circ$:l=0.5. Dotted line with $\square$:l=0.3. The vertical lines to the left of each curve show the velocities at which the time to topological transformation should diverge to infinity (since steadily propagating lenses are possible below these velocities): Solid line: l=0.9. Long-dashed line: l=0.7. Short-dashed line: l=0.5. Dotted line: l=0.3.

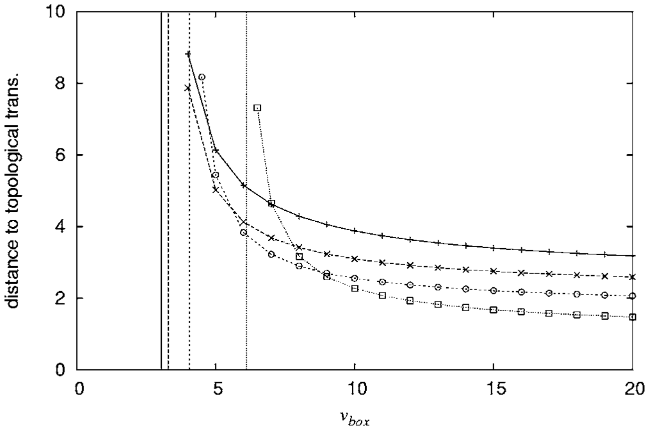

FIG. 15. Distance along the channel (in units of one channel width) for the occurrence of the topological transformation (lens bubble detaching from the spanning film) as a function of the driving velocity v_{box} for rapidly driven systems that have no steady state. The initial condition upon start up of the driving velocity was the equilibrium lens structure. Various lens sizes are shown: solid line with $+$:l=0.9. Long-dashed line with $\times$:l=0.7. Short-dashed line with $\circ$:l=0.5. Dotted line with $\square$:l=0.3. The vertical lines to the left of each curve show the velocities at which the distance to topological transformation should diverge to infinity (since steadily propagating lenses are possible below these velocities): Solid line: l=0.9. Long-dashed line: l=0.7. Short-dashed line: l=0.5. Dotted line: l=0.3.

face energy E (Fig. 9) are *decreasing* functions of driving pressure p_b.

Note that according to the discussion in Sec. VI A, as v_{box} approaches the maximum allowed value for which steady solutions are available (at any given l) the characteristic rate of approach to steady state should become vanishingly small. This is because the eigenvalue governing that rate of approach becomes zero. Under those circumstances it can take an extremely long time for the system to approach its final steady state.

C. Loss of stability

Now consider suddenly imposed driving velocities v_{box} sufficiently high that no steady-state solution could exist. Again the equilibrium lens structure is used as the initial condition with various l values being examined.

As expected, over time the lens structure breaks apart via a topological transformation: the lens bubble and spanning film detach from each other. This breakup process is an inherently dynamic one. For given l and v_{box}, it is achieved in a finite time and at a finite distance along the channel. Moreover, the configurations seen on the route to the topological transformation do not correspond to steady states for any set of parameter values.

Figures 14 and 15, respectively, show the dimensionless time to achieve the topological transformation and the dimensionless distance at which it occurs, as functions of the driving velocity v_{box}. The dimensionless time scale has already been defined in Sec. III (see also Appendix B). The dimensionless distance is easy to understand: it is merely distance along the channel measured in units of one channel width.

For values of v_{box} just in excess of critical, the time and distance to achieve the topological transformation tend to diverge: this is as might be expected. The system is only marginally unstable, and the characteristic growth rate of the instability is low.

This argument can be made more explicit by considering the evolution of the shape of the lens structure to be a trajectory in a function space consisting of all possible shapes. Consider two cases, both starting from an equilibrium lens, one with v_{box} slightly less than critical and one with v_{box} slightly greater than critical. Even though the eventual fates of two such trajectories will be very different, the trajectories themselves should be continuous with v_{box}. In other words, they can be kept close together (according to some measure of distance in the function space) over any chosen time interval, merely by choosing the respective v_{box} values sufficiently close either side of the critical value. Recall that all the simulations of subcritical trajectories (starting from the equilibrium lens) have been found to approach the steady solution branch according to the discussion in Sec. VII B and that slightly subcritical trajectories should approach steady state (a fixed point in the function space) exceedingly slowly. It follows that trajectories with the same initial state but with slightly supercritical v_{box} values should be held up for extremely long times in the same neighborhood of the function space, before eventually running away to a topological transformation.

In any case, as v_{box} increases further above the critical value, the time to achieve transformation decreases. Meanwhile, the distance to achieve the transformation (which is simply time multiplied by v_{box}) also decreases; it appears to be a slowly decreasing function in the limit of large imposed v_{box}.

The behavior of time (and distance) to topological transformation with respect to the lens size l is interesting: in most cases (i.e., for sufficiently large v_{box}), smaller l values tend to need less time and distance to break up the structure. This may seem counterintuitive at first as smaller lenses are "harder to break" in the sense that steady solutions only break down at higher imposed back pressures and velocities. However, it should be remembered that the topological transformation requires the vertex (at which the three films meet) to migrate from its original equilibrium position to the top of the channel. The smaller the lens, the less distance the vertex must migrate before the transformation occurs. It is only as v_{box} decreases somewhat that the time and distance to break smaller lenses in Figs. 14 and 15 overtake their larger-lens counterparts, since the former are approaching the regime where they can propagate steadily and indefinitely without breaking up.

We have already described the state of the system after the topological transformation (Sec. VI A). Specifically this is a flat spanning film crossing the entire channel and propagating along it, with a stationary semicircular bubble being left behind (see Fig. 11). The semicircular bubble cannot be flushed out of the channel merely by blowing harder. However, if the spanning film is blown back in the opposite direction, it will reattach to the bubble, reproducing the lens structure, which can then be blown forward again. In this manner bubbles, which may have been trapped on channel walls, can be flushed out of the channel.

VIII. CONCLUSIONS

The viscous froth model is a valuable tool for elucidating the physics that governs flowing foams, incorporating the balance between pressure, surface-tension-induced curvature forces, and viscous drag. The inclusion of viscous drag in the model means it is capable of resolving rapid processes, such as fast-flowing foam rheology and foam relaxation after a topological transformation. Without any viscous drag term, it would only be possible to address quasistatic deformation of foams, while topological transformations could be represented merely as discrete jumps in the foam configuration. With viscous terms included, any topological transformations can be fully resolved, but whether and when they occur depends on the rate at which the foam is flowing or deforming: this conclusion seems to be robust across a range of model systems and experimental geometries [21,28,31,32,34].

In this work, the viscous froth model has been applied to a very simple geometrical configuration of a two-dimensional foam flowing along a channel: this configuration is called a lens structure. It consists of a lens-shaped bubble contacting one channel wall and extending part of the way across the channel, with an additional film, known as the spanning film, connecting from the lens-shaped bubble to the opposite channel wall. Thus altogether there are just three films in the structure.

Even for a configuration this simple, the viscous froth model is revealed to have a very rich dynamics. There is an equilibrium state of the lens structure, but the system can be driven out of equilibrium by imposing a driving pressure behind it. The structure then deforms and migrates along the channel.

The behavior of the system can be described parametrically in terms of two dimensionless parameters: a lens size parameter l (the fraction of the channel width which the equilibrium lens bubble extends across the channel) and the dimensionless driving pressure p_b (made dimensionless based on film tension and channel width). Given these state parameters, the system response can be described in terms of various geometric and dynamical properties of the structure, such as the cross-channel displacement of the vertex (at which the three films meet), the rotation or turning angle of the vertex (relative to the equilibrium state), the distribution of curvature along films, the steady migration velocity of the structure along the channel (assuming the structure eventually attains a steady state), the pressure in the lens bubble itself, and the total energy of the structure (equal to the total film length in our dimensionless system).

Perturbation results for steady-state migration can be obtained in the limit of "small" driving pressures p_b. These results are valid over a restricted pressure range for large- or medium-size lens bubbles, but up to quite high $O(l^{-1/2})$ dimensionless pressures for small $l \ll 1$ lenses. Beyond these range(s), numerical steady-state solutions can be obtained.

The vertex does not displace at all in the cross-channel direction according to the weakly driven theory. For higher driving pressures the vertex displaces toward the lens bubble, flattening that bubble along the channel wall and also extending the spanning film. The results of the weakly driven theory suggest that lens structures with both small and large lens bubbles resist vertex rotation: the stiffness to rotation arises in the former case from the small lens bubble and in the latter case from the short spanning film. However, the symmetry between vertex rotation or turning angles for the small and large lens bubble cases breaks down as the driving back pressure grows. Thus, as the vertex displaces and the spanning film stretches, the large-lens-bubble case becomes much more compliant and rotates considerably more than its small-lens-bubble counterpart. The distribution of curvature along the spanning film producing the vertex rotation is also interesting: it tends to be uniform for weakly driven structures, but confined to a boundary layer near the vertex for strongly driven ones.

Structures with small lens bubbles migrate faster than those with large lens bubbles: this is because small lens bubble structures have less overall length of film and hence less drag. The adverse effect of a large lens bubble on mobility of the structure can be mitigated somewhat for high back pressures by displacing the vertex to extend the spanning film (thereby replacing two films by a single one across much of the channel width) and by flattening the lens bubble somewhat along the channel wall: the more that films of the lens bubble reorient parallel to the channel wall, the less drag they incur during propagation.

The pressure in the lens bubble is augmented (relative to the equilibrium pressure) by at least half the back pressure.

Bubble pressures and film lengths are closely coupled in the viscous froth model, and the pressure increase for a weakly driven lens bubble reflects an important symmetry property of the films in this limit. One film of the lens bubble grows and the other shrinks: at leading order these changes cancel. The spanning film likewise only curves but does not extend at leading order in weakly driven systems. As we have said, the system energy is the overall film length of the entire structure (including all three films). While this exhibits no leading-order change for weak back pressures, rapid growth in energy is seen for larger back pressures on larger-size lens bubbles.

The above conclusions refer to lens structures propagating at steady state. However, we have observed that there is a critical back pressure (and associated critical velocity) beyond which steady solutions cease to exist. This critical pressure is (mostly) a decreasing function of lens size l. At the critical pressure, stability is lost and the structure runs away to a topological transformation: the lens bubble detaches from the spanning film. The lens bubble is then left behind in the channel, while the spanning film propagates forward.

Returning to the situation below the critical back pressure, an unsteady-state simulation has revealed that the steady solutions we have considered previously are stable: hence if the structure is disturbed in some way, it will return to steady state. Although we have not formulated the problem as such, it should be possible to decompose any deformation away from steady state in terms of a series of eigenmodes. The eigenvalue associated with the least stable eigenmode will control the ultimate rate of approach back to steady state. A second branch of steady solutions (believed to be unstable) has also been identified. For each lens size, it joins the original steady branch at the critical back pressure. At the point where these two branches meet, the rate associated with the least stable deformation mode must fall to zero.

Above the critical back pressure (or technically above the associated critical velocity), we have simulated both the time to run away to a topological transformation and the distance along the channel at which the topological transformation takes place. Just slightly above the critical velocity, the time to achieve a topological transformation and hence the corresponding distance are arbitrarily large. The time and distance to achieve the topological transformation decrease as the velocity imposed on the lens structure grows, distance to topological transformation, in particular, being a slowly decreasing function of imposed velocity.

In summary, the dynamics of the viscous froth model is surprisingly complex even for a structure with as few as three films. The behavior of the model in a foam consisting of a multitude of films is likely to be more fascinating still.

APPENDIX A: FOAM CONFINED BETWEEN GLASS PLATES

It is generally considered that a foam confined between two closely spaced glass plates can be treated as effectively two dimensional. The precise details of how this comes about are quite subtle and require a good understanding of the forces on foam films, as we now describe. Instead of the dimensionless variables used almost exclusively throughout the main text, we shall employ dimensional variables in the following discussion: this will help to make the force balance arguments we describe somewhat clearer.

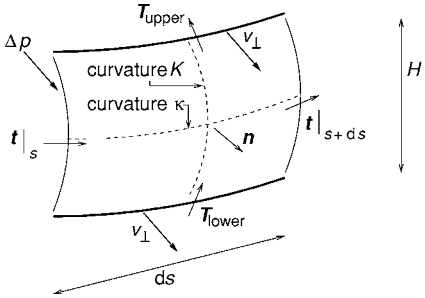

FIG. 16. A segment of length ds of moving foam film. The film is confined between plates separated by a distance H, with the plate separation being much smaller than the total film length. For clarity the plates are not actually shown in the figure. The film has a curvature K in the direction across the plates and a curvature κ along them. These curvatures are associated with spatial changes in film tangents $\boldsymbol{T}$ and $\boldsymbol{t}$, respectively, the changes in $\boldsymbol{T}$ being between upper and lower plates (see $\boldsymbol{T}_{upper}$ and $\boldsymbol{T}_{lower}$ in the figure) and those in $\boldsymbol{t}$ being between positions along the film s and $s+ds$. These spatial changes in the tangents, coupled with surface tension, lead to forces on the film. A pressure difference Δp across the film also produces force. At the plates, the film edges swell into Plateau border channels (indicated as bold curves in the figure). These channels incur viscous drag forces, according to their rate of motion over the plates $v_\perp$ (a projection of their velocity in the direction of the film normal $\boldsymbol{n}$, which is a vector in the plane of the plates and at right angles to $\boldsymbol{t}$). Consideration of separate force balances on the upper plate, on the lower plate and on the film segment excluding the plate regions, can be used to derive the two-dimensional viscous froth model.

We consider a moving foam film (see Fig. 16) confined between two closely spaced plates with the thickness of the gap between the plates denoted H. We suppose the length of the foam film is many times larger than H. The film shape is somewhat analogous to the interface shape that arises during two-phase displacement in Hele-Shaw cells [47]: specifically the moving film can billow like a sail and will have a curvature both along the plates (denote this κ) and across the plates (denote this K). These curvatures are associated with spatial changes in film tangent directions, respectively, for tangents $\boldsymbol{t}$ (along the plates) and $\boldsymbol{T}$ (across the plates). Throughout the main text we focused exclusively on κ and $\boldsymbol{t}$. Our aim here is to show how terms involving K and $\boldsymbol{T}$ can be eliminated from consideration.

The viscous froth model can be derived by considering a length ds along the plates of the billowing film. The film segment swells into channels (so-called Plateau borders) adjacent to the plates themselves. We consider a force balance on three separate regions of the film segment across the thickness between the plates: the Plateau border channel region at the upper plate, the analogous region at the lower plate, and the remaining space between the plates (which accounts for the bulk of the film, the Plateau border regions being small compared to H).

1. Force balance at the upper plate

There is a surface tension force acting on the upper-plate Plateau border region that depends on the curvature K. Specifically we are interested in the amount that the tangent $\boldsymbol{T}_{upper}$ deviates from the vertical owing to this curvature. We therefore need to project the surface tension force in the direction $\boldsymbol{n}$, which is a vector in the plane of the plates, but normal to $\boldsymbol{t}$. The projected surface tension force on the Plateau border element of length ds is $-2\sigma\boldsymbol{T}_{upper}\cdot\boldsymbol{n}\,ds$: the sign convention for $\boldsymbol{T}$ is chosen such that (for an undeformed film) $\boldsymbol{T}$ would point from the lower to the upper plate.

This surface tension force must be balanced to a drag force. Drag occurs when the motion of the film projected in the direction $\boldsymbol{n}$ is nonzero: denote this normal film speed by $v_{\perp}$. Suppose that the motion of the swollen channel across the upper plate is characterized by a linear friction law with drag coefficient (per element length) ζ_{upper}. We then deduce

$$\zeta_{upper}v_{\perp} = -2\sigma\boldsymbol{T}_{upper}\cdot\boldsymbol{n}. \tag{A1}$$

No pressure forces appear in Eq. (A1). This is because pressure forces require a finite area over which to act, but the thickness of the swollen channel region at the plate is considered to be arbitrarily small compared to the spacing H between the confining plates. For a similar reason there are no surface tension forces associated with changes in the tangent $\boldsymbol{t}$ appearing in Eq. (A1): this is because such forces require a finite height over which to act.

2. Force balance at the lower plate

A similar force balance can be applied to the swollen channel region around the lower plate, where the relevant tangent direction is $\boldsymbol{T}_{lower}$ and the relevant drag coefficient is ζ_{lower}. According to our sign convention,

$$\zeta_{lower}v_{\perp} = 2\sigma\boldsymbol{T}_{lower}\cdot\boldsymbol{n}. \tag{A2}$$

Note in particular that ζ_{lower} is not necessarily the same as ζ_{upper} since under the action of gravity, the swollen channels might be thicker on the lower plate compared to the upper plate. For a foam liquid fraction of ε confined between the plates, the capillary suction pressure into the swollen channels will be on the order of $\sigma/(\varepsilon^{1/2}H)$. Meanwhile, the liquid hydrostatic pressure difference between upper and lower plates will be $\rho g H$, where ρ is the liquid density and g is the gravitational acceleration. Utilizing physical and geometric properties from a recently reported experiment [36], $\sigma=27\times10^{-3}$ N m^{-1}, $\rho=1000$ kg m^{-3}, $g=9.8$ m s^{-2}, and $H=3$ mm, the ratio between the capillary suction and hydrostatic pressures (for a relatively dry foam with $\varepsilon=0.01$) is around 3. Based on the value of this ratio, moderate differences between channels on upper and lower plates might be expected, but large order-of-magnitude differences between them (and hence between ζ_{upper} and ζ_{lower}) are ruled out.

3. Force balance across the bulk of the film

It remains to write a normal force balance on the element of film (length ds, height H) between the plates, but excluding the Plateau border regions at the plates. Surface tension forces $2\sigma\boldsymbol{T}_{upper}\cdot\boldsymbol{n}\,ds$ and $-2\sigma\boldsymbol{T}_{lower}\cdot\boldsymbol{n}\,ds$ apply at above and below, respectively. On the sides of the film element, forces $2\sigma H\boldsymbol{t}|_{s+ds}$ and $-2\sigma H\boldsymbol{t}|_{s}$ apply: since $d\boldsymbol{t}/ds\equiv-\kappa\boldsymbol{n}$, the net normal force component is $-2\sigma\kappa H\,ds$. Meanwhile, the normal pressure force (for a film pressure difference Δp) is $\Delta pH\,ds$. All these forces must sum to zero: no dissipative forces enter the force balance, since these only occur near the plates, a region we have explicitly excluded. We deduce

$$0 = \Delta pH - 2\sigma\kappa H + 2\sigma\boldsymbol{T}_{upper}\cdot\boldsymbol{n} - 2\sigma\boldsymbol{T}_{lower}\cdot\boldsymbol{n}. \tag{A3}$$

4. Derivation of the viscous froth model

If we substitute Eqs. (A1) and (A2) into Eq. (A3), then divide through by H, and define an overall drag coefficient $\zeta=(\zeta_{upper}+\zeta_{lower})/H$, we obtain the two-dimensional viscous froth equation given originally in Eq. (1). In particular the difference between $\boldsymbol{T}_{upper}$ and $\boldsymbol{T}_{lower}$ terms (which depends on the cross-plate film curvature K) has been eliminated from the governing equation, in favor of frictional drag terms, which can be represented (via the overall drag coefficient ζ) in a wholly two-dimensional way.

APPENDIX B: TYPICAL SCALES FOR THE VISCOUS FROTH LENS

The vast majority of the results considered in this work have been cast in dimensionless form. This appendix gives the conversions back to dimensional variables, to enable a better appreciation of the scales on which the predicted phenomena might occur.

We base our estimates around an apparatus used for a two-dimensional foam channel flow experiment that was reported recently [36]. The apparatus was a channel of width $L=9$ mm, confined by Plexiglas plates, with a thickness between the plates (which we shall denote H) of $H=3$ mm. The liquid used to make the foam was a water-surfactant-glycerol mixture with viscosity $\mu=1.16\times10^{-3}$ Pa s and surface tension $\sigma=27\times10^{-3}$ N m^{-1}. Although this experiment only used a modest amount of glycerol (5% by volume), raising the viscosity only slightly above that of water, generally speaking, mixing glycerol into a water-surfactant mixture is a useful experimental strategy when one wants to observe out-of-equilibrium foams. Large departures from equilibrium are only observed when the imposed deformation rate exceeds the viscous relaxation rate and become more accessible if the relaxation time is increased via higher liquid viscosity.

Values of velocity along the channel of "a few centimeters per second" have been reported in the above-mentioned experiment [36]. Suppose a typical speed, which we denote v_{typ}, is 0.025 m s^{-1}. Since the capillary number is defined as

$$\mathrm{Ca} = \mu v/\sigma, \tag{B1}$$

a typical capillary number (denoted Ca_{typ}) is $\mathrm{Ca}_{typ}\approx0.0010$. Clearly the capillary number is a small parameter.

The main complication in estimating the dimensional scales for the viscous froth lens system concerns finding a suitable value of the viscous drag parameter ζ. This is because a drag law that is linear in velocity is not strictly appropriate.

The physical reason for this is the complicated hydrodynamics of a Plateau border sliding over a plate. Most of the dissipation is confined in a so-called transition region near the Plateau border of thickness $\mathrm{Ca}^{2/3}$ (relative to the interplate spacing) and extent $\mathrm{Ca}^{1/3}$ along the plates (again relative to the interplate spacing) [47,48]. The typical shear stress in this region is of order $\mu v_{typ}/(\mathrm{Ca}_{typ}^{2/3}H)$, and if it is integrated over the order $\mathrm{Ca}_{typ}^{1/3}H$ region extent, the drag force per length of Plateau border is order $\mu v_{typ}\mathrm{Ca}_{typ}^{-1/3}$. Clearly by Eq. (B1) this is simply $\sigma\mathrm{Ca}_{typ}^{2/3}$.

We wish to convert this to a drag force per unit channel cross section, which is easily achieved by multiplying by the Plateau border perimeter and dividing by cross sectional area. For a single flat film (as opposed to a lens structure) propagating along the channel, drag per cross-sectional area equates to the driving film pressure difference, for which an equation is known from literature [36]. We hence deduce

$$\zeta v_{typ} = \frac{38(2L)}{LH}\sigma\mathrm{Ca}_{typ}^{2/3} = \frac{76}{H}\sigma\mathrm{Ca}_{typ}^{2/3} \Rightarrow \zeta = 76\frac{\mu}{H}\mathrm{Ca}_{typ}^{-1/3}, \tag{B2}$$

where 38 is an experimentally observed coefficient, $2L$ is essentially the Plateau border perimeter (assuming a large aspect ratio limit for simplicity), and LH is channel cross section. Substituting in values quoted previously we find $\zeta \approx 290\ \mathrm{kg\ m^{-2}\ s^{-1}}$.

Although this value of ζ strictly applies only when $v = v_{typ}$ or equivalently when $\mathrm{Ca}=\mathrm{Ca}_{typ}$, we shall assume a linear drag law where a constant ζ applies over a wide range of velocities: from Eq. (B2) it is clear that ζ is in any case a weak function of capillary number.

An additional cause for uncertainty in the value of ζ is that the experimental result [Eq. (B2)] gives a drag that is an order of magnitude greater than some theoretical analyses. In order to minimize any possible confusion surrounding the validity of Eq. (B2), we briefly summarize the findings of the theoretical analyses here. Specifically if $\mathcal{P}$ is the Plateau border perimeter, the predictions are

$$\zeta v = \frac{\bar{\lambda}\mathcal{P}}{LH}\sigma\mathrm{Ca}^{2/3}, \tag{B3}$$

where $\bar{\lambda}$ is a geometric factor equal to 1.8 for a square channel [36,41], 2.1 for a channel with $L=2H$, and 5.0 for a channel with $L \gg H$ [41]. Note that the value $\bar{\lambda}=3.8$ is often associated with the $L \gg H$ case [47], but this only applies to drag from the front of a bubble: the quoted value 5.0 incorporates drag from the rear of the bubble also [41]. The reason Eq. (B3) appears to give substantially lower drag than Eq. (B2) is believed to be due to surfactant effects [36]. The theory assumes tangential stress-free bubble boundaries, whereas experiments (on the basis of which our quoted ζ value has been estimated) have Marangoni stresses making boundaries somewhat more rigid. Indeed in the extreme case of tangentially immobile bubble surfaces [37] powers of Ca other than those suggested by Eqs. (B2) and (B3) may arise.

In any case, now that ζ has been estimated via Eq. (B2), the velocity $2\sigma/(L\zeta)$ and time scales $L^2\zeta/(2\sigma)$ defined in the main text (see Sec. III) can be estimated. These evaluate, respectively, to $0.020\ \mathrm{m\ s^{-1}}$ (which is sufficiently close to the above quoted $v_{typ}=0.025\ \mathrm{m\ s^{-1}}$ for our estimate of ζ to be valid) and 0.43 s [which could be resolved on a charge-coupled-device (CCD) camera recording 25 images per second as in previous experiments [36]]. Remember that this characteristic time scale controls both rate of approach to the steady-state lens structure (when one exists) and rate of break up of the structure (when stability is lost). As already alluded to above, even longer characteristic times could be achieved by mixing more glycerol into the foaming fluid. In summary the velocity and time scales we have predicted for phenomena in the viscous froth lens system seem compatible with typical laboratory experiment scales.

APPENDIX C: UNSTEADY-STATE AREA CONSTRAINT

Equation (25) is an area constraint for the lens. In unsteady-state viscous froth computations it would be normal to replace this constraint by a condition that $\dot{A}_l=0$. For the lens this can be written (using the same subscript notation for back and front films as in the main text)

$$\int_b v_\perp ds = \int_f v_\perp ds. \tag{C1}$$

After invoking Eqs. (6) and (7) and using the known turning angles $\frac{\pi}{3} \pm \delta\phi$ of the back and front films, this can be manipulated [31] into the form

$$p_l\mathcal{L}_f + (p_l - p_b)\mathcal{L}_b = \frac{2\pi}{3}, \tag{C2}$$

where $\mathcal{L}_b$ and $\mathcal{L}_f$ are the back and front film lengths. This is the usual form of the pressure equation used in unsteady-state viscous froth simulations (we return to using dimensionless variables here) and it could be used to find p_l for a given p_b if instantaneous film lengths were known.

In order to see mathematically why the above equations are inadequate for steady-state computations, we proceed as follows. For a steady state, uniform migration velocity v, we have $v_\perp = v\cos\phi$ by Eq. (8) and $dy=\cos\phi\, ds$ [see the discussion preceding Eq. (10)]. Thus Eq. (C1) reduces to

$$\int_b v\, dy = \int_f v\, dy. \tag{C3}$$

Canceling the constant v from both sides merely reproduces one of the constraints in Eq. (23): namely, that matching the front and back films at the vertex. No new mathematical constraint is implied by Eq. (C1). The physical reason for this is that a condition that rate of change of lens area vanishes in the steady state is *not* sufficient to ensure strict area conservation: it is also necessary to ensure that area does not change at all times *on the approach* to steady state. Thus purely steady-state calculations, which only address the final steady version of Eq. (C2), must additionally impose Eq. (25).

APPENDIX D: NUMERICAL PROCEDURES FOR THE STEADY-STATE LENS

Here we discuss the numerical procedures used to solve the constraint equations (23)–(25) for the steady-state lens. Solutions can be found by a Newton-Raphson technique [45]. However, the right-hand side of constraint (25) generally needs to be obtained via a quadrature (specifically we used Simpson's rule with an adaptive step size to keep error within a specified tolerance), rather than by an analytic formula. As a result of this, Jacobians, which are required by the Newton-Raphson technique, are computed numerically.

Depending on the solution branch of interest, either the perturbation theory of Sec. IV or the nearly detached lens theory of Sec. VI B will provide excellent starting guesses for the Newton-Raphson technique. The back pressure can then be increased in small increments, using the solution from the previous increment as the Newton-Raphson guess for the next. The solution can be carried as far as is desired, *provided the branch of steady-state solutions continues to exist*.

We have also used an independent computational method (see Appendix D 1 below) as a check on the results, obtaining identical solutions in both cases.

1. Shooting method

As a check on the results for the steady-state lens structure, we have also used another independent technique for computing the lens configuration subject to a finite back pressure p_b. The technique is the so-called shooting method [45]. It has the advantage that it avoids the somewhat tedious integrations needed to obtain Eqs. (18)–(21).

In order to set up the method we first need to define a vector film position $\boldsymbol{x}(s)$, a tangent $\boldsymbol{t} \equiv d\boldsymbol{x}/ds$, and a normal $\boldsymbol{n}$, being the clockwise rotation of the tangent through $\frac{\pi}{2}$. As s is measured upwards in our notation, $\boldsymbol{t}$ has a upward pointing component and $\boldsymbol{n}$ has a forward pointing component.

We now employ the definition of curvature: namely,

$$d^2\boldsymbol{x}/ds^2 = d\boldsymbol{t}/ds \equiv -\kappa\boldsymbol{n}, \tag{D1}$$

to deduce from Eqs. (6) and (8)

$$d^2\boldsymbol{x}/ds^2 = (v\cos\phi - \Delta p)\boldsymbol{n}, \tag{D2}$$

where $\cos\phi$ is obtained as the projection of $\boldsymbol{t}$ onto the vertical.

Given p_b we guess the values of $\delta\phi$, p_l, and v.

We start the integration off for the spanning film at the bottom of the channel, where $\boldsymbol{t}$ is known to be vertical. We integrate Eq. (D2), using a second-order accurate integration scheme with a fixed step size for s (chosen, after tests for convergence, to be 5×10^{-4}), until $\boldsymbol{t}$ turns through the guessed angle $\delta\phi$. The final step of the integration for this film needs an adjustment of step size so as to achieve the required turning angle exactly, but this is easy to determine as the tangent is known at both the start and end of the final step.

Now the tangent is turned through an angle $\pm\frac{\pi}{3}$ and we integrate along the back and front films. We can stop the integration once the film coordinates equal (or exceed) the channel width. Tangent directions at the top of the channel can be obtained by interpolating over this final step.

The extent to which the constraints have been violated is determined by the amount that the tangents at the channel top deviate from vertical on both front and back films and by any violation of the lens area constraint. A Newton-Raphson scheme is employed adjusting the guessed $\delta\phi$, p_l, and v values so as to ensure the constraint violations vanish. Jacobians required by the Newton-Raphson scheme are computed numerically. Again the scheme can be started off at low p_b values (for which the weakly driven lens perturbation theory supplies excellent guesses) and carried forward to higher p_b, using each solution obtained as a starting guess for the next one.

Although the scheme is slower to execute than the one described previously, computing constraint violations via a detailed numerical procedure, rather than a more straightforward function evaluation and/or simple quadrature, it nonetheless provides an excellent, independent check on any results obtained.

APPENDIX E: ALGORITHMS FOR THE UNSTEADY-STATE LENS

The algorithm we used to simulate the unsteady-state viscous froth is similar to one already in the literature [31] but with a number of innovations to improve its performance. These innovations are concerned with (i) improving the spatial accuracy of the algorithm, (ii) improving the handling of film end points, (iii) improving the temporal accuracy of the algorithm, and (iv) avoiding undesired stretching or shrinking of film segments.

1. Discretization of the films

Each film $\boldsymbol{x}(s)$ is discretized into a finite number of points: given that unsteady-state simulations are expensive, we chose a modest number of such points, only around 20–50 points *on average* per film (contrast the steady-state computations in Appendix D 1. Subject to the discretization, our target is to describe geometric properties along the film: i.e., tangent vector $\boldsymbol{t}$, normal vector $\boldsymbol{n}$, and curvature κ, with a spatial accuracy up to second order in the discretization. Improving the spatial accuracy from first to second order not only reduces the memory requirements of a simulation (as a given film can be tracked accurately using fewer discrete points and segments), but also the simulation time (curvature is known to diffuse along films in the viscous froth model [30], so that permissible simulation time increments are bounded by the square of the spatially discretized film segment lengths, as is standard in diffusive problems [45]). Conversely, going beyond second-order spatial accuracy is prohibitively awkward, as it would no longer be permitted to approximate distance along the film as the sum of the straight line lengths for each discrete segment.

Film tangents $\boldsymbol{t}$ at any selected film point are evaluated via a weighted sum of the unit vectors along the directions of the segments connecting the film point to its two neighbors. If the segments are of unequal length, the *shorter* segment receives a higher weight in the sum: this weighting (not employed in previous formulations [31]) ensures that the film tangent at each film point is computed with second-order spatial accuracy. Film normals $\boldsymbol{n}$ are then computed by rotating the film points through $\frac{\pi}{2}$.

The second derivative of film position with respect to length along the film—i.e., $d^2\boldsymbol{x}/ds^2$—is computed by taking a finite difference of the tangent vector with respect to tangents at neighboring film points. If segments happen to be of unequal length, a weighted average of the finite differences is used, weighted to shorter segments as before. If the tangent vectors were exact, this would give a second-order accurate approximation to $d^2\boldsymbol{x}/ds^2$. In fact, since the tangents themselves are finite-difference approximations, in a worst case only first-order accuracy for $d^2\boldsymbol{x}/ds^2$ is obtained. The curvature $\kappa = -\boldsymbol{n}\cdot d^2\boldsymbol{x}/ds^2$ would then be obtained at the same level of accuracy.

Second-order accuracy can only be achieved in general by (i) calculating second derivatives explicitly in terms of nearest- and next-nearest-neighbor film points with carefully chosen weightings or (ii) retaining the formula that employs a finite difference of tangent vectors, but invoking more accurate approximations to the film tangents, which themselves incorporate more distant film points.

Neither of these are particularly attractive options from the point of view of a simulation, as penultimate film points—i.e., those neighboring the end point of each film—need special treatment (as they only have next-nearest neighbors on one side and not the other).

However, fortunately, second-order accuracy is also recovered in the special case where adjacent film segments are of equal length. This is not a trivial point, as under the viscous froth model, the distance between film material points evolves over time. Even if film segments are chosen to be equal length initially, their lengths will become unequal as time progresses. The options are either a regular regridding to equalize the segment lengths and/or some other strategy to prevent discrete segments from stretching or shrinking in the first place. Specifically our regridding algorithm imposed the minimum point separation to be 0.01 and the maximum point separation to be 0.05, destroying or creating points, respectively, in case these minima (maxima) were violated. Sensitivity to the precise minimum (maximum) separations employed was low. Additional strategies were, however, put in place to reduce the need for regridding, at least for systems not undergoing any topological transformation: these strategies will be addressed later in Appendix E 4.

Obviously in cases involving topological transformation (see, e.g., Sec. VII C) one film shrinks away to nothing and regridding cannot be entirely avoided. In the computations, films always had, in addition to their end points, at least one interior point. As a result, topological transformations were assumed to occur when the film length shrank to twice the minimum point separation.

2. Locating film end points

The viscous froth model [Eq. (6)] describes the dynamic evolution of points interior to a film, but film end points are instead determined via a constraint—namely, that films must meet threefold at $\frac{2\pi}{3}$ angles and must meet channel walls at right angles.

We shall consider how to incorporate these constraints in a simulation, focusing primarily on the threefold meeting angle constraint (the treatment of the right-angle constraint at channel walls may be handled similarly).

In the lens structure consider the three films (back, front, and spanning) and, specifically, the film points that are nearest neighbors to the so-called vertex at which the films meet.

As a first approximation, straight lines can be drawn from the nearest-neighbor film points into the vertex to meet at $\frac{2\pi}{3}$ angles. This is a classical mathematical problem known as Steiner's problem [49–54]: the vertex is the so-called Steiner point of the triangle formed by the nearest-neighbor film points. There are several geometric constructions [55,56] enabling the Steiner point to be located: elementary coordinate geometry on these constructions then yields an explicit formula for the Steiner point.

The Steiner point, however, is only an approximation to the true vertex location. It has been located by assuming that films are straight lines between the vertex and nearest-neighbor film points. In reality our discretized film points are approximations to a true underlying curved film, with the film tangent varying continuously along each of the curves.

The $\frac{2\pi}{3}$ meeting angle rule really applies to the film tangents evaluated at the vertex, not to film secants joining the vertex to nearest-neighbor film points (which is what the Steiner point technique produces). Accurate positioning of the vertex at each increment of time is essential to ensure that curvatures at film points neighboring the vertex are computed correctly, these curvatures subsequently affecting the evolution of film point location for later-time increments.

The effects of film curvature at and/or near the vertex can be incorporated as follows. Suppose we guess the (unknown) vertex position $\boldsymbol{x}_v$. For each film, a unique parabola can then be obtained interpolating the guessed vertex position and the known nearest- and next-nearest-neighbor film points. Then the tangents to each parabola are obtained at the guessed $\boldsymbol{x}_v$, each tangent being a known function in terms of the guessed $\boldsymbol{x}_v$. Owing to the sense in which we measure arc length s (i.e., from below), the spanning film tangent $\boldsymbol{t}_s$ points into the vertex, while the back and front film tangents $\boldsymbol{t}_b$ and $\boldsymbol{t}_f$ point away. If $\boldsymbol{x}_v$ has been guessed correctly, then

$$\boldsymbol{t}_s = \boldsymbol{t}_b + \boldsymbol{t}_f. \tag{E1}$$

The correct vertex position can be obtained by applying a Newton-Raphson technique [45] to solve Eq. (E1) for $\boldsymbol{x}_v$. The Steiner point provides an excellent starting guess to the value of $\boldsymbol{x}_v$, so that rapid Newton-Raphson convergence is guaranteed.

3. Update of film point positions

We have already described in Appendix E 1 the challenges concerned with obtaining second-order spatial accuracy. Now we address the issue of temporal accuracy.

Related to this is the issue of ensuring that the area constraint [Eq. (25)] remains satisfied. Ideally Eq. (C2) would be sufficient to ensure this: in practice, truncation errors in the numerical scheme may lead over time to a secular drift in the lens area away from the correct value. Such drifts are well known in simulations of other physical systems subject to constraints [57,58] and require that a strategy be adopted in the simulation algorithm to counteract any drift and explicitly enforce the constraint.

Previous work on the viscous froth model [31] employed an explicit first-order temporal scheme. This can be improved using a predictor-corrector method, with a first-order predictor and second-order corrector. The predictor-corrector technique (discussed below) is fully compatible with the vertex locator algorithm discussed in Appendix E 2: it is simply necessary to apply that algorithm upon each predictor and corrector step.

Suppose $\{\boldsymbol{x}\}$ denotes a set of discrete film points, while $\{\boldsymbol{n}\}$ and $\{\kappa\}$ are, respectively, normal vectors and curvatures evaluated at these film points (as described in Appendix E 1). We adopt subscripts (0), (p), and (c) to denote, respectively, the state at the beginning of a time step, the predicted state at the end of a time step, and the corrected state at the end of a time step. The duration of the time step is δt (which we chose to be 10^{-4} dimensionless time units given our roughly 20–50 points per film spatial resolution). Suppose that bubble pressures are computed at the beginning of a time step using Eq. (C2), pressure differences across films $\Delta p_{(0)}$ thus being obtained.

The predictor step (as used in previous studies [31]) is

$$\{\boldsymbol{x}_{(p)}\} = \{\boldsymbol{x}_{(0)}\} + \boldsymbol{n}_{(0)}(\Delta p_{(0)} - \{\kappa_{(0)}\})\,\delta t. \tag{E2}$$

This may, however, lead to an area constraint violation. Previous work [31] has shown how to correct this area violation by considering a generalized version of Eq. (C2), which describes bubbles that can change their area by coarsening driven by gas diffusion across films. This equation when applied to the lens structure yields

$$p_l\mathcal{L}_f + (p_l - p_b)\mathcal{L}_b = \frac{2\pi}{3} + \dot{A}_l. \tag{E3}$$

If the area increases spuriously by some amount during a step, it can be corrected by setting $\dot{A}_l$ in Eq. (E3) to cancel the spurious increase. Previously [31] with a first-order temporal scheme, the correction for any particular time step was only applied on the following step, by which stage yet another spurious area change could have accumulated. However, we effect the correction within the time step itself by assigning predictor pressures according to the area violation (denoted $\delta A_{(p)}$) incurred during the predictor step, which may be computed using the set of film points $\{\boldsymbol{x}_{(p)}\}$ from Eq. (E2) and associated lengths (denoted $\mathcal{L}_{(p)}$) for each film. Specifically we have

$$p_{l(p)}\mathcal{L}_{f(p)} + (p_{l(p)} - p_b)\mathcal{L}_{b(p)} = \frac{2\pi}{3} - \frac{2\,\delta A_{(p)}}{\delta t}, \tag{E4}$$

from which predicted film pressure differences $\Delta p_{(p)}$ can be obtained, assuming the imposed back pressure p_b is fixed. The case we actually solved, for which the rate of advance of the lens structure averaged across the channel (rather than p_b) was fixed, is only very slightly more complicated mathematically. We shall not give details here, but note that again predicted pressures at the end of the step can be readily obtained.

Given the predicted film pressure differences $\Delta p_{(p)}$, a corrector equation can be applied, giving better estimates of film point positions at the end of the step:

$$\{\boldsymbol{x}_{(c)}\} = \{\boldsymbol{x}_{(0)}\} + \boldsymbol{n}_{(0)}(\Delta p_{(0)} - \{\kappa_{(0)}\})\frac{\delta t}{2} + \boldsymbol{n}_{(p)}(\Delta p_{(p)} - \{\kappa_{(p)}\})\frac{\delta t}{2}. \tag{E5}$$

By construction $\{\boldsymbol{x}_{(c)}\}$ will violate the constraints to a much lesser extent than $\{\boldsymbol{x}_{(p)}\}$. The reason that $-2\delta A_{(p)}/\delta t$, rather than just $-\delta A_{(p)}/\delta t$, appears on the right-hand side of Eq. (E4) is that the predictor pressure only applies for half the time step in Eq. (E5) to obtain $\{\boldsymbol{x}_{(c)}\}$.

A corrected lens pressure can now be obtained via an analog of Eq. (E4) and yet more improvements in $\{\boldsymbol{x}_{(c)}\}$ values found using an analog of Eq. (E5). This process can be applied iteratively until the area constraint violation is arbitrarily small. Multiple iterations are generally unnecessary, however: the only requirement is that the constraint violation be less than the difference between the true area of a bubble with curved films and the polygonal representation of the bubble using discretized segments.

4. Controlling the behaviour of film segments

In Appendix E 1 we have already discussed the importance of keeping film points on discretized films relatively evenly spaced so as to obtain second-order or near-second-order spatial accuracy for estimates of film curvature. In this section we consider the reasons for film points *failing* to maintain even spacing and the strategies for correcting this. The strategy we ultimately adopt has an elegant physical interpretation, is simple to implement, and automatically maintains even film point spacing as steady state (if it exists) is reached.

a. Film segment growth and shrinkage

Consider a differential segment of film $d\boldsymbol{x}$, which we suppose to be a material element. Applying Eq. (6) the rate at which this segment evolves is

$$\dot{d\boldsymbol{x}} = d(\Delta p - \kappa)\boldsymbol{n} + (\Delta p - \kappa)d\boldsymbol{n} = -\,d\kappa\,\boldsymbol{n} + (\Delta p - \kappa)\kappa\boldsymbol{t}\,ds. \tag{E6}$$

where we have used the fact that Δp is uniform along the film and $d\boldsymbol{n}/ds = \kappa\boldsymbol{t}$. Since the segment length ds satisfies $ds = \boldsymbol{t}\cdot d\boldsymbol{x}$, we deduce via Eq. (E6)

$$\dot{ds} = \boldsymbol{t}\cdot\dot{d\boldsymbol{x}} = (\Delta p - \kappa)\kappa\,ds. \tag{E7}$$

Since $\Delta p \neq \kappa$ for the viscous froth in general, $\dot{ds}$ is nonzero. Moreover, since κ varies along the films of the lens structure in general, $\dot{ds}$ also varies along films. Clearly different material elements stretch and/or shrink at different rates over time.

b. Introducing artificial tangential motion

The viscous froth model as stated in Eq. (6) only associates drag with normal film motion, not with any sliding motion of points along films. Indeed *any* artificial tangential dynamics can be added to the model without film shapes being affected and therefore without model predictions being altered in any way. In other words, the discretized segments used to represent films in simulations no longer need to correspond to material elements (contrast Appendix E 4 a), but rather may slide tangentially relative to them.

Suitably chosen tangential dynamics can help to keep segments between film points roughly uniform, allowing second-order spatial accuracy of curvatures to be approached. One possibility to achieve this is to allow the film points to repel one another. The stronger the repulsive force, the more uniform the segments remain. However, stronger repulsive forces also speed up the artificial tangential dynamics. Small time steps must then be chosen to resolve the tangential motion, meaning that simulations to address the (normal) dynamics of real interest become exceedingly expensive. This feature is well known in other systems for which nearly equal spacing of elements is maintained by strong or stiff forces [57,58]. It is far more practical to compute the rate of tangential stretching or shrinkage according to Eq. (E7) and apply a tangential velocity that simply offsets it.

If the viscous froth model, incorporating some extra artificial tangential motion v_{art}, is written in vector form as

$$\boldsymbol{v} = (\Delta p - \kappa)\boldsymbol{n} + v_{art}\boldsymbol{t}, \tag{E8}$$

then one proposal for the specific form of the tangential motion is

$$dv_{art}/ds = -(\Delta p - \kappa)\kappa, \tag{E9}$$

which can be shown to result in $\dot{ds}=0$. For the lens structure, Eq. (E9) can be solved subject to vanishing v_{art} at the point where each film meets the channel walls: as the films meet the channels at right angles, such points then move exclusively along the channel walls.

Equations (E8) and (E9) are *not* in fact the ones we solve. Instead we treat a rather similar system of equations, which we discuss in the next subsection.

c. Sliding matchbox foam vs the growing back bubble

In Sec. VII C we mentioned that the unsteady-state problem we actually solved was that sketched in Fig. 13, which we called a sliding matchbox system. This corresponds to confining a foam between plates and then sliding the plates (to the left at some speed v_{box}) over a barrier.

Here we will demonstrate explicitly the analogy already alluded to in Sec. VII A between the sliding matchbox system and one in which plates are fixed but the back bubble grows at a constant rate $\dot{A}_b$. We will also demonstrate a significant computational advantage of the sliding matchbox foam: namely, that it has an automatic tendency to compensate for growth and shrinkage of film material elements mentioned in Appendix E 4 a and E 4 b.

Consider, for the sliding matchbox system, the dynamics of the foam between the plates. Viscous froth equation (6) of course only describes the foam film motion relative to the plates. The film motion relative to the laboratory frame, which we denote $\boldsymbol{V}$, obeys

$$\boldsymbol{V} = (\Delta p - \kappa)\boldsymbol{n} - v_{box}\boldsymbol{e}_x = (\Delta p - \kappa - v_{box}\boldsymbol{e}_x \cdot \boldsymbol{n})\boldsymbol{n} - v_{box}(\boldsymbol{e}_x \cdot \boldsymbol{t})\boldsymbol{t}. \tag{E10}$$

We are free to add in any artificial motion along film tangents [cf. Eq. (E8)]. Specifically we choose to add in $v_{box}(\boldsymbol{e}_x \cdot \boldsymbol{t})\boldsymbol{t}$ to produce in place of Eq. (E10):

$$\boldsymbol{V} = (\Delta p - \kappa - v_{box}\boldsymbol{e}_x \cdot \boldsymbol{n})\boldsymbol{n}; \tag{E11}$$

i.e., motion in the laboratory frame is entirely normal to the film.

In the main text (Sec. VII) we stated that the simulations were performed in a situation where the confining plates slide over a barrier, with the back bubble (located between the barrier and the lens structure) being fixed in size; i.e., no gas can cross either the barrier or the lens structure. This was compared with a situation with no imposed plate sliding, but where the rate of advance of the lens structure averaged across the channel was fixed; i.e., the back bubble behind the lens grew at a constant rate. However, the two situations—i.e., sliding plates and a back bubble of constant size versus stationary plates and a growing back bubble—are completely analogous.

Consider the general equation for rate of change of back bubble size *written in the frame of the plates*. The barrier has unit length and advances at speed v_{box} in this frame (consuming back bubble area). Meanwhile, the so-called back and spanning films of the lens advance (augmenting area): only the normal velocity is relevant in producing area changes, and in the frame of the plates this is $\Delta p - \kappa$ regardless of whether laboratory frame motion via Eq. (E10) or (E11) is applied. Using these facts, we can express

$$\dot{A}_b = -v_{box} + \int_s v_\perp ds + \int_b v_\perp ds \tag{E12}$$

in the form

$$\dot{A}_b = -v_{box} + \int_s (\Delta_s p - \kappa) ds + \int_b (\Delta_b p - \kappa) ds, \tag{E13}$$

where we have employed the subscript notation used in the main text (see, e.g., Secs. III A and III B). By comparing two situations in Eq. (E13), the growing back bubble $\dot{A}_b \neq 0$ with no plate sliding $v_{box}=0$, and the fixed size back bubble $\dot{A}_b=0$ with a nonzero v_{box}, the analogy is made explicit: the same pressures are found in each case.

The sliding matchbox system is a somewhat more convenient one to analyze than the original system with its constantly growing back bubble. The film shapes computed by the sliding matchbox system can be thought of as corresponding to those that would be seen in the original system by a camera moving along with the growing back bubble. As a result, the steady state of Eq. (E11) is simply $\boldsymbol{V}=0$: there is no normal motion and hence no further shape distortion.

The sliding matchbox system is therefore ideally suited to simulations that aim to describe the relaxation of a lens structure to steady state. It is very easy to judge when steady state has been achieved: $\boldsymbol{V}$ must vanish (within some tolerance) at all points along the film.

It is also simple to demonstrate that Eq. (E11) gives no shrinkage or stretching of film segments at steady state: since $\boldsymbol{V}$ vanishes for each and every film point, the differential velocity $d\boldsymbol{V}$ across a film segment of length ds also vanishes. Hence $\dot{ds}=\boldsymbol{t}\cdot d\boldsymbol{V}$ must be zero.

The sliding matchbox system is a significant improvement in computational terms over the original viscous froth equation (6) for which tangential stretching and shrinking of elements continues indefinitely. Although some regridding may still be necessary early on to correct inequities that develop in segment lengths, the rate at which regridding needs to be applied decreases dramatically as steady state is approached.

---

[1] A. M. Kraynik, Annu. Rev. Fluid Mech. **20**, 325 (1988).
[2] D. Weaire and M. A. Fortes, Adv. Phys. **43**, 685 (1994).
[3] D. Weaire and S. Hutzler, *The Physics of Foams* (Clarendon Press, Oxford, 1999).
[4] F. Graner, Y. Jiang, E. Janiaud, and C. Flament, Phys. Rev. E **63**, 011402 (2001).
[5] A. M. Kraynik, D. A. Reinelt, and F. van Swol, Phys. Rev. E **67**, 031403 (2003).
[6] Y. Jiang, P. J. Swart, A. Saxena, M. Asipauskas, and J. A. Glazier, Phys. Rev. E **59**, 5819 (1999).
[7] H. M. Princen, J. Colloid Interface Sci. **91**, 160 (1983).
[8] D. Weaire and J. P. Kermode, Philos. Mag. B **50**, 379 (1984).
[9] A. M. Kraynik and M. G. Hansen, J. Rheol. **30**, 409 (1986).
[10] T. Herdtle and H. Aref, J. Fluid Mech. **241**, 233 (1992).
[11] S. J. Neethling and J. J. Cilliers, Powder Technol. **101**, 249 (1999).
[12] T. Okuzono and K. Kawasaki, Phys. Rev. E **51**, 1246 (1995).
[13] D. A. Reinelt and A. M. Kraynik, J. Colloid Interface Sci. **159**, 460 (1993).
[14] D. A. Reinelt and A. M. Kraynik, J. Fluid Mech. **311**, 327 (1996).
[15] A. M. Kraynik, D. A. Reinelt, and F. van Swol, in *Proceedings of the Third Euroconference on Foams, Emulsions and their Applications (Eurofoam 2000), Delft, Netherlands, 2000*, edited by P. Zitha, J. Banhart, and G. Verbist (Verlag Metall Innovation Technologie MIT, Bremen, 2000), pp. 191–198.
[16] D. A. Reinelt and A. M. Kraynik, J. Rheol. **44**, 453 (2000).
[17] P. Grassia, J. J. Cilliers, and S. J. Neethling, Can. J. Phys. **79**, 1265 (2001).
[18] P. Grassia, Philos. Mag. Lett. **83**, 403 (2003).
[19] A. D. Gopal and D. J. Durian, J. Colloid Interface Sci. **213**, 169 (1999).
[20] A. D. Gopal and D. J. Durian, Phys. Rev. Lett. **91**, 188303 (2003).
[21] F. Rouyer, S. Cohen-Addad, M. Vignes-Adler, and R. Höhler, Phys. Rev. E **67**, 021405 (2003).
[22] D. J. Durian, Phys. Rev. E **55**, 1739 (1997).
[23] S. Tewari, D. Schiemann, D. J. Durian, C. M. Knobler, S. A. Langer, and A. J. Liu, Phys. Rev. E **60**, 4385 (1999).
[24] D. A. Reinelt and A. M. Kraynik, J. Fluid Mech. **215**, 431 (1990).
[25] F. Elias, C. Flament, J. A. Glazier, F. Graner, and Y. Jiang, Philos. Mag. B **79**, 729 (1999).
[26] D. Weaire and J. P. Kermode, Philos. Mag. B **48**, 245 (1983).
[27] D. J. Durian, Phys. Rev. Lett. **75**, 4780 (1995).
[28] I. Cantat and R. Delannay, Phys. Rev. E **67**, 031501 (2003).
[29] J. A. Glazier and D. Weaire, J. Phys.: Condens. Matter **4**, 1867 (1992).
[30] D. Weaire and S. McMurry, Solid State Phys. **50**, 1 (1997).
[31] N. Kern, D. Weaire, A. Martin, S. Hutzler, and S. J. Cox, Phys. Rev. E **70**, 041411 (2004).
[32] S. Cox, D. Weaire, and J. A. Glazier, Rheol. Acta **43**, 442 (2004).
[33] S. J. Cox, in *Proceedings of the 5th European Conference on Foams, Emulsions and Applications, EUFOAM 2004, University of Marne-la-Vallée, Champs sur Marne, France, 2004*, edited by M. Vignes-Adler, D. Weaire, and R. Miller [Colloids Surf., A **263**, 81 (2005)].
[34] W. Drenckhan, S. J. Cox, G. Delaney, H. Holste, D. Weaire, and N. Kern, Colloids Surf., A **263**, 52 (2005).
[35] L. W. Schwartz and H. M. Princen, J. Colloid Interface Sci. **118**, 201 (1987).
[36] I. Cantat, N. Kern, and R. Delannay, Europhys. Lett. **65**, 726 (2004).
[37] N. D. Denkov, V. Subramanian, D. Gurovich, and A. Lips, Colloids Surf., A **263**, 129 (2005).
[38] N. D. Denkov, S. Tcholakova, K. Golemanov, V. Subramanian, and A. Lips, *A collection of papers in honor of Professor Ivan B. Ivanov (Laboratory of Chemical Physics, University of Sofia) celebrating his contributions to colloid and surface science on the occasion of his 70th birthday*, edited by P. A. Kralchevsky and N. D. Denkov. [Colloids Surf., A **282-283**, 329 (2006)].
[39] A. Saugey, W. Drenckhan, and D. Weaire, Phys. Fluids **18**, 053101 (2006).
[40] D. Reinelt, P. Boltenhagen, and N. Rivier, Eur. Phys. J. E **4**, 299 (2001).
[41] H. Wong, C. J. Radke, and S. Morris, J. Fluid Mech. **292**, 95 (1995).
[42] H. Wong, C. J. Radke, and S. Morris, J. Fluid Mech. **292**, 71 (1995).
[43] A. Peleg, B. Meerson, A. Vilenkin, and M. Conti, Phys. Rev. E **63**, 066101 (2001).
[44] W. Drenckhan (personal communication).
[45] W. H. Press, S. A. Teukolsky, W. T. Vetterling, and B. P. Flannery, *Numerical Recipes in C: The Art of Scientific Computing*, 2nd ed. (Cambridge University Press, Cambridge, England, 1992) 2nd ed.
[46] K. T. Alligood, T. D. Sauer, and J. A. Yorke, *Chaos: An Introduction to Dynamical Systems* (Springer-Verlag, Berlin, 1996).

[47] C. W. Park and G. M. Homsy, J. Fluid Mech. **139**, 291 (1984).
[48] F. P. Bretherton, J. Fluid Mech. **10**, 166 (1961).
[49] A. O. Ivanov and A. A. Tuzhilin, *Minimal Networks: The Steiner Problem and its Generalizations* (CRC Press, Boca Raton, 1994).
[50] R. Courant and H. Robbins, *What is Mathematics? An Elementary Approach to Ideas and Methods* (Oxford University Press, Oxford, 1969).
[51] C. Isenberg, *The Science of Soap Films and Soap Bubbles* (Dover, Mineola, NY, 1992).
[52] S. Hildebrandt and A. Tromba, *Mathematics and Optimal Form* (Scientific American Books, San Francisco, 1985).
[53] P. Winter, Networks **17**, 129 (1987).
[54] E. N. Gilbert and H. O. Pollak, SIAM J. Appl. Math. **16**, 1 (1968).
[55] S. Gueron and R. Tessler, Am. Math. Monthly **109**, 443 (2002).
[56] J. Tong and Y. S. Chua, Math. Mag. **98**, 214 (1995).
[57] P. Grassia, E. J. Hinch, and L. C. Nitsche, J. Fluid Mech. **282**, 373 (1995).
[58] P. Grassia and E. J. Hinch, J. Fluid Mech. **308**, 255 (1996).